

## RESEARCH ARTICLE SUMMARY

## NEUROSCIENCE

## Connectomic comparison of mouse and human cortex

Sahil Loomba<sup>†</sup>, Jakob Straehle<sup>†</sup>, Vijayan Gangadharan<sup>†</sup>, Natalie Heike<sup>†</sup>, Abdelrahman Khalifa<sup>†</sup>, Alessandro Motta<sup>†</sup>, Niansheng Ju, Meike Sievers, Jens Gempt, Hanno S. Meyer, Moritz Helmstaedter\*<sup>\*</sup>

**INTRODUCTION:** The analysis of the human brain is a central goal of neuroscience, but for methodological reasons, research has focused on model organisms, the mouse in particular. Because substantial homology was found at the level of ion channels, transcriptional programs, and basic neuronal types, a strong similarity of neuronal circuits across species has also been assumed. However, a rigorous test of the configuration of local neuronal circuitry in mouse versus human—in particular, in the gray matter of the cerebral cortex—is missing.

The about 1000-fold increase in number of neurons is the most obvious evolutionary change of neuronal network properties from mouse to human. Whether the structure of the local cortical circuitry has changed as well is, however, unclear. Recent data from transcriptomic analyses has indicated an increase in the proportion of inhibitory interneurons from mouse to human. But what the effect of such a change

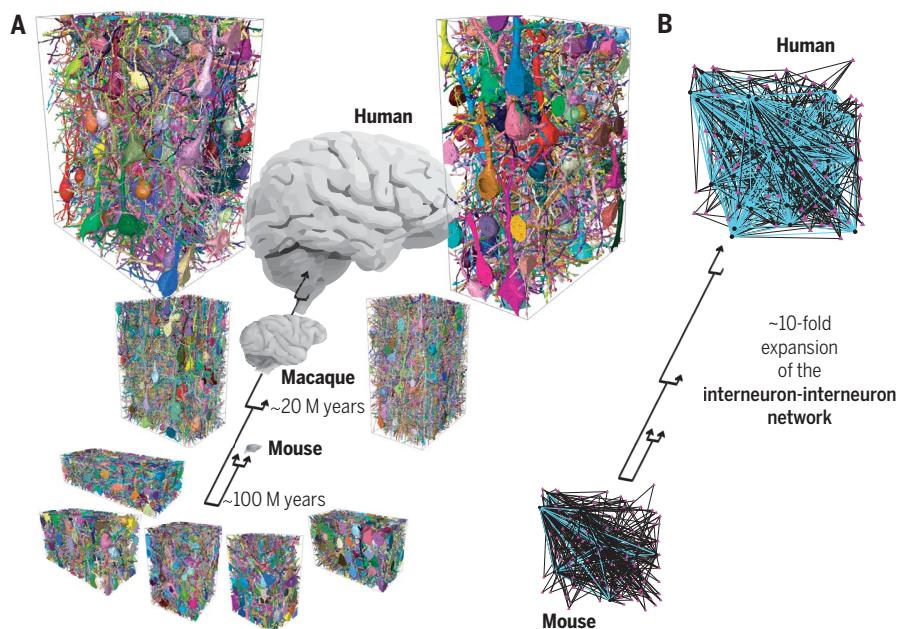
is on the circuit configurations found in the human cerebral cortex is not known. This is, however, of particular interest also to the study of neuropsychiatric disorders because in these, the alteration of inhibitory-to-excitatory synaptic balance has been identified as one possible mechanistic underpinning.

**RATIONALE:** We used recent methodological improvements in connectomics to acquire data from one macaque and two human individuals, using biopsies of the temporal, parietal, and frontal cortex. Human tissue was obtained from neurosurgical interventions related to tumor removal, in which access path tissue was harvested that was not primarily affected by the underlying disease. A key concern in the analysis of human patient tissue has been the relation to epilepsy surgery, when the underlying disease has required often year-long treatment with pharmaceuticals, plausibly altering syn-

aptic connectivity. Therefore, the analysis of nonepileptic surgery tissue seemed of particular importance. We also included data from one macaque individual, who was not known to have any brain-related pathology.

**RESULTS:** We acquired three-dimensional electron microscopy data from temporal and frontal cortex of human and temporal and parietal cortex of macaque. From these, we obtained connectomic reconstructions and compared these with five connectomes from mouse cortex. On the basis of these data, we were able to determine the effect of the about 2.5-fold expansion of the interneuron pool in macaque and human cortex compared with that of mouse. Contrary to expectation, the inhibitory-to-excitatory synaptic balance on pyramidal neurons in macaque and human cortex was not substantially altered. Rather, the interneuron pool was selectively expanded for bipolar-type interneurons, which prefer the innervation of other interneurons, and which further increased their preference for interneuron innervation from mouse to human. These changes were each multifold, yielding in effect an about 10-fold expanded interneuron-to-interneuron network in the human cortex that is only sparsely present in mouse. The total amount of synaptic input to pyramidal neurons, however, did not change according to the threefold thickening of the cortex; rather, a modest increase from about 12,000 synaptic inputs in mouse to about 15,000 in human was found.

**CONCLUSION:** The principal cells of the cerebral cortex, pyramidal neurons, maintain almost constant inhibitory-to-excitatory input balance and total synaptic input across 100 million years of evolutionary divergence, which is particularly noteworthy with the concomitant 1000-fold expansion of the neuronal network size and the 2.5-fold increase of inhibitory interneurons from mouse to human. Rather, the key network change from mouse to human is an expansion of almost an order of magnitude of an interneuron-to-interneuron network that is virtually absent in mouse but constitutes a substantial part of the human cortical network. Whether this new network is primarily created through the expansion of existing neuronal types, or is related to the creation of new interneuron subtypes, requires further study. The discovery of this network component in human cortex encourages detailed analysis of its function in health and disease. ■



**Connectomic screening across mammalian species: Comparison of five mouse, two macaque, and two human connectomic datasets from the cerebral cortex.** (A) Automated reconstructions of all neurons with their cell bodies in the volume shown, using random colors. The analyzed connectomes comprised a total of ~1.6 million synapses. Arrows indicate evolutionary divergence: the last common ancestor between human and mouse, approximately 100 million years ago, and the last common ancestor between human and macaque, about 20 million years ago. (B) Illustration of the about 10-fold expansion of the interneuron-to-interneuron network from mouse to human.

The list of author affiliations is available in the full article online.

\*Corresponding author. Email: mh@brain.mpg.de

†These authors contributed equally to this work.

Cite this article as S. Loomba et al., *Science* **377**, eabo0924 (2022). DOI: 10.1126/science.abo0924

**S** READ THE FULL ARTICLE AT  
<https://doi.org/10.1126/science.abo0924>

## RESEARCH ARTICLE

## NEUROSCIENCE

## Connectomic comparison of mouse and human cortex

Sahil Loomba<sup>1,2†</sup>, Jakob Straehle<sup>1,†‡§</sup>, Vijayan Gangadharan<sup>1,¶</sup>, Natalie Heike<sup>1,†</sup>, Abdelrahman Khalifa<sup>1,†</sup>, Alessandro Motta<sup>1,†</sup>, Niansheng Ju<sup>1</sup>, Meike Sievers<sup>1,2</sup>, Jens Gempt<sup>3</sup>, Hanno S. Meyer<sup>3</sup>, Moritz Helmstaedter<sup>1\*</sup>

The human cerebral cortex houses 1000 times more neurons than that of the cerebral cortex of a mouse, but the possible differences in synaptic circuits between these species are still poorly understood. We used three-dimensional electron microscopy of mouse, macaque, and human cortical samples to study their cell type composition and synaptic circuit architecture. The 2.5-fold increase in interneurons in humans compared with mice was compensated by a change in axonal connection probabilities and therefore did not yield a commensurate increase in inhibitory-versus-excitatory synaptic input balance on human pyramidal cells. Rather, increased inhibition created an expanded interneuron-to-interneuron network, driven by an expansion of interneuron-targeting interneuron types and an increase in their synaptic selectivity for interneuron innervation. These constitute key neuronal network alterations in the human cortex.

**T**he human brain, with its 86 billion nerve cells (1) forming a network of unparalleled complexity, is of special interest for neuroscience. Yet over the past 50 years, rodents (in particular, the mouse) have emerged as key research subjects, offering methodological opportunities not available for the study of the human brain. Because at the molecular level evolutionary homology is substantial for ion channels, synaptic receptors, and other key molecular constituents of the brain, similar homology has been assumed for neuronal circuits, especially in the cerebral cortex. However, comparative synaptic-resolution connectomic studies of mouse and human cortex are required to determine the degree to which circuit structure may have evolved between species.

Detailed studies of the human cerebral cortex have provided data on cellular composition of the neuropil (1–14), synaptic properties (15–25), and neuronal morphology (14, 26–28), yielding a comparative description with reference to rodents that indicates a larger number of glial cells (2), larger synapses (20, 29, 30), and more inhibitory interneurons (INs) (4, 9) to form the neuronal network of the human cortex. This latter comparison had been confounded by rodent data reporting an IN fraction of 8 to

25%, (3, 4, 31–37), thus potentially on par with data from primates (range 15 to 37%) (38–42). Recent transcriptomic data substantiates an at least twofold increase (4, 9), suggesting the balance between inhibitory and excitatory synapses to be substantially shifted toward inhibition. Furthermore, on the basis of the about threefold larger extent of the dendritic trees of human pyramidal cells, it has been assumed that human cortical neurons receive substantially more synapses than those of rodents (for example, 10,000 in rodents versus 30,000 in human) (29, 43–46).

However, a circuit-level analysis of the human cortex that addresses the potential effect of multifold increased inhibitory circuit elements is still missing. Would, as a result, the inhibitory-to-excitatory synaptic balance be increased in the human cortex? Because inhibitory-to-excitatory synaptic balance has emerged as a key set point that might be altered in neuropsychiatric diseases [studied primarily in mouse models (47, 48)], this question is relevant for the healthy and diseased human brain.

We used three-dimensional (3D) electron microscopy (EM) followed by sparse and dense circuit reconstruction (49) to map the synaptic and cellular composition of layer 2/3 (L2/3) in mouse, macaque, and human cortex. Sampling from multiple individuals and cortical regions, we screened for key connectomic alterations between mouse and human cortex, which a single dataset from a given human individual and disease condition would not have allowed (10). Although our human data was from diseased individuals who underwent neurosurgical interventions, the patients had not undergone yearlong treatment for epileptic disorders that could have substantially altered the synaptic network. By including

additional data from macaque in our study, we furthermore could ensure that none of the reported effects was exclusively attributable to a diseased state of the human brain. We determined the circuit effects of an expanded inhibitory neuron population in the human cortex and obtained a quantitative picture of the human pyramidal cell synaptic input architecture.

## Results

We obtained tissue samples (Fig. 1) from the cerebral cortex of two human individuals (a 69-year-old female and an 80-year-old male) who underwent neurosurgical operations (access tissue that had to be removed during surgery and would have been discarded otherwise) (Materials and methods) and of one rhesus macaque (*Macaca mulatta*, 15.6-year-old male). Individual ages corresponded to 83, 102, and 52% of statistical life expectancy, respectively.

From these tissue samples, we acquired 3D EM image datasets in cortical L2/3 using either serial blockface EM (SBEM) (50) [macaque primary somatosensory cortex (S1) dataset sized 176 by 224 by 100  $\mu\text{m}$ ; superior temporal gyrus (STG) sized 175 by 225 by 108  $\mu\text{m}$ ; human (H5) STG sized 166 by 216 by 112  $\mu\text{m}$ , and human (H6) inferior frontal gyrus (IFG) sized 170 by 215 by 79  $\mu\text{m}$ , all at a voxel size of 11.24 by 11.24 by (28 to 30) nm] or automated tape-collecting ultramicrotome multiple scanning EM (ATUM-multiSEM) (51–53) [dataset human (H5) STG spanning all cortical layers, sized 1.7 mm by 2.1 mm by 28.3  $\mu\text{m}$  and dataset from the same sample focused on L2/3 sized 1.1 mm by 1.1 mm by 82  $\mu\text{m}$  (total 0.41 PB of data) both at a voxel size of 4 by 4 by (35 to 40) nm]. For comparison with mouse cortex, we densely reconstructed (49, 54) previously published 3D EM datasets from L2/3 of S1, secondary visual (V2), posterior parietal (PPC), and anterior cingulate (ACC) cortical areas (55) and acquired an additional dataset from mouse secondary auditory cortex (A2) sized 115 by 175 by 109  $\mu\text{m}$ , approximately corresponding to the location of the STG datasets from macaque and human. In the following, we report effects that were multifold between mouse ( $n = 5$  individuals,  $n = 5$  cortical regions) and macaque or human ( $n = 3$  individuals,  $n = 4$  cortical regions).

**Inhibitory versus excitatory neuronal composition**

The fraction of nerve cells that were INs increased 2.5-fold between mouse and macaque or human [ $n = 88$  of 734 versus 278 of 914 neurons from  $n = 5$  mouse and  $n = 4$  macaque and human datasets pooled,  $P < 0.001$  (Materials and methods)] (Fig. 2, A and B), which is consistent with recent reports from transcriptomic cell type analyses (4, 9). This change in the neuronal composition of cortical tissue could have profound effects on the synaptic input to pyramidal (excitatory) neurons (ExNs)

<sup>1</sup>Department of Connectomics, Max Planck Institute for Brain Research, Frankfurt, Germany. <sup>2</sup>Faculty of Science, Radboud University, Nijmegen, Netherlands. <sup>3</sup>Department of Neurosurgery, Klinikum rechts der Isar, School of Medicine, Technical University of Munich, Munich, Germany.

\*Corresponding author. Email: mh@brain.mpg.de

†These authors contributed equally to this work.

‡Present address: Department of Neurosurgery, University Freiburg, Freiburg, Germany.

§Present address: Berta-Ottenstein Clinician Scientist Program, Faculty of Medicine, University Freiburg, Freiburg, Germany.

¶Present address: Institute for Vascular and Islet Cell Biology, German Diabetes Center, Leibniz Center for Diabetes Research at Heinrich Heine University Düsseldorf, Düsseldorf, Germany.

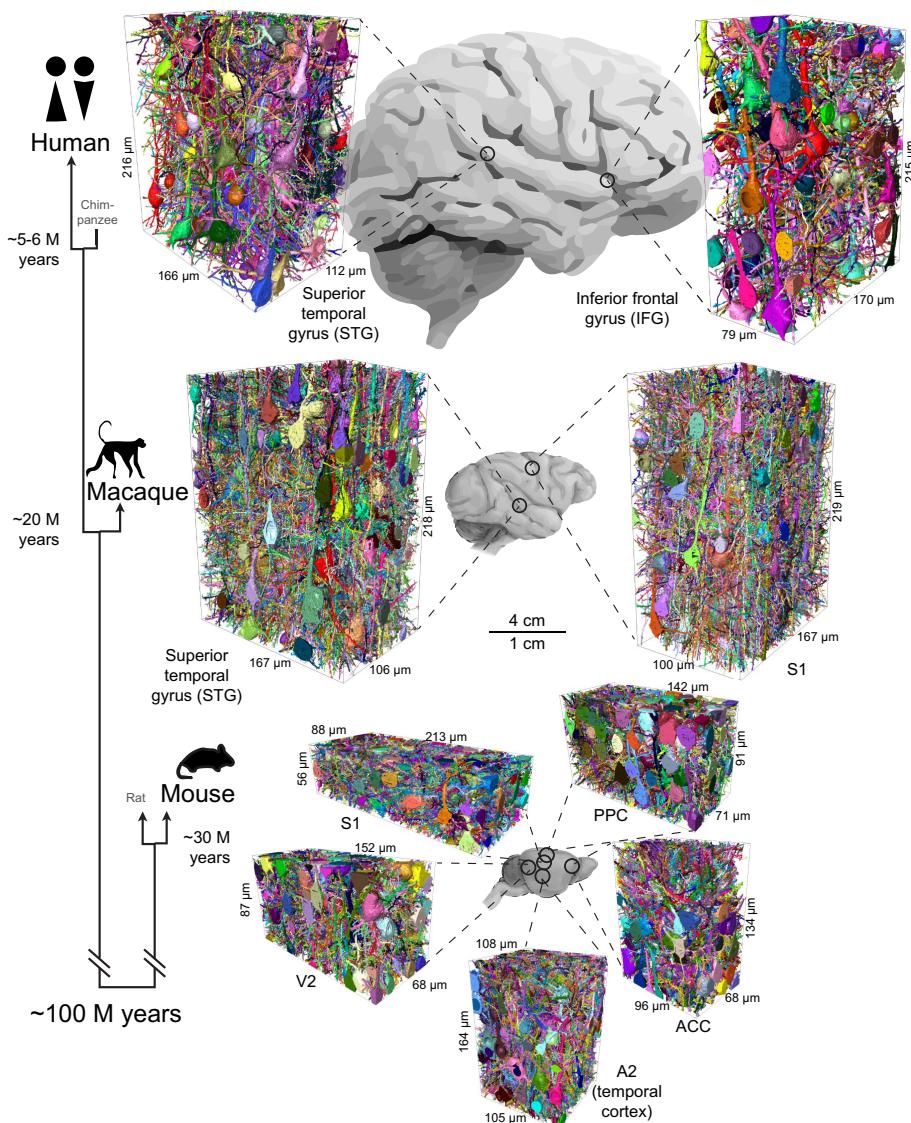


**Fig. 1. Comparative connectomic analysis of mouse, macaque, and human cortex.** Dense connectomic reconstructions from L2/3 of five cortical areas of mouse (bottom,  $n = 5$  individuals) and from four cortical areas of macaque and human ( $n = 3$  individuals). There are matched cortical areas (A2 and STG) across all three species and paired samples from S1 (mouse and macaque). A total of 202,954 axons and 1,618,129 synapses were analyzed (Materials and methods). The raw 3D EM data of mouse datasets S1, V2, PPC, and ACC were previously published (55), but their dense reconstruction have not. (Left) Simplified phylogenetic tree [based on (100)] indicating time to last common ancestor between human (*Homo sapiens*), rhesus macaque (*Macaca mulatta*), and mouse (*Mus musculus*). Scale bars apply to the brain sketches. S1, primary somatosensory cortex; A2, secondary auditory cortex; V2, secondary visual cortex; PPC, posterior parietal cortex; ACC, anterior cingulate cortex; STG, superior temporal gyrus; IFG, inferior frontal gyrus.

(Fig. 2C): If all other circuit properties were unchanged between mouse and human, the inhibitory-to-excitatory balance (i/e balance) would also be 2.5-fold shifted toward inhibition compared with that in mouse.

#### Synaptic inputs to pyramidal cell dendrites

We therefore first analyzed the synaptic input to pyramidal cell dendrites in mouse, macaque, and human (Fig. 2, D to H). Although the density of synapses onto the dendritic shaft of

pyramidal cells remained largely constant from mouse to macaque and only slightly increased in human [ $0.16 \pm 0.13$  per micrometer of dendritic shaft length versus  $0.17 \pm 0.11$  and  $0.21 \pm 0.08$ ;  $n = 46, 36$ , and  $49$ ;  $P = 0.6$  and  $P = 0.003$  for mouse to macaque and mouse to human, respectively; Kolmogorov-Smirnov (KS) test; mean  $\pm$  SD] (Fig. 2, D and E), synapses onto dendritic spines were 2.7-fold sparser in macaque and human [ $1.99 \pm 0.65$  per micrometer of dendritic shaft length

(mouse) versus  $0.86 \pm 0.36$  (macaque) and  $0.67 \pm 0.25$  (human); mean  $\pm$  SD;  $n = 46, 36$ , and  $49$ , respectively;  $P < 10^{-18}$ , KS test mouse versus macaque and human] (Fig. 2, D and E). As a result, the fraction of synapses made onto the dendritic shafts of pyramidal cells (out of all input synapses to these dendrites) was increased 2.7-fold ( $n = 1111$  synapses, mouse and  $n = 1638$  synapses macaque and human,  $P < 0.001$ , KS test) (Fig. 2, F and H). Synaptic inputs to spine necks, stubs, or double innervation of dendritic spines were rare but slightly increased in macaque and human (Fig. 2G; statistics are provided in the caption).

In mouse, synapses onto dendritic spines have been reported to be predominantly excitatory (49, 56) and synapses onto dendritic shafts predominantly inhibitory (55, 57, 58). Therefore, the finding of a 2.7-fold increased fraction of shaft synapses could indicate a substantial shift in the set point for the i/e balance in human [as recently claimed for nonhuman primate (59)]. For this to be correct, however, the properties of excitatory and inhibitory axons—in particular, their preference for establishing synapses onto dendritic shafts and spines—would have to remain unaltered between mouse and macaque and human. We investigated this next (Figs. 3 and 4).

#### Synaptic properties of excitatory and inhibitory neurons

We first reconstructed axons of pyramidal cells and INs in mouse and human (Fig. 3, A to C) to determine their synaptic preferences. The rate of spine innervation showed the well-documented dichotomy in mouse (Fig. 3, A and B) (49, 55, 60): Pyramidal cell axons targeted dendritic spines with  $61.47 \pm 9.26\%$  (mean  $\pm$  SD) of their output synapses ( $n = 11$  axons,  $n = 367$  output synapses), whereas INs only very rarely made an output synapse as the only synapse onto a dendritic spine ( $n = 1$  of 263 IN output synapses in mouse), with no overlap between the populations. In human, however, axons reconstructed from the cell bodies of pyramidal cells made only  $30.37 \pm 16.16\%$  (mean  $\pm$  SD) of their output synapses onto dendritic spines ( $n = 15$  axons,  $n = 1126$  output synapses), whereas INs maintained their almost complete exclusion of single spine innervation (Fig. 3, B and C) [ $n = 12$  axons,  $n = 345$  output synapses, of which  $n = 1$  were single spine synapses; IN axons did, however, innervate dendritic spines as double innervations, in all species, as reported for subtypes of INs (fig. S3) (61–63); only the single spine innervation rate was used for the following analyses]. Thus, the distributions of synaptic target properties between pyramidal and IN axons reconstructed from their cell body of origin were less separated in human (Fig. 3B) and indicated a change in axonal synaptic preference from mouse to human.

**Fig. 2. Multifold changes in cellular composition and synaptic input of mouse versus macaque and human cortex.**

(A and B) Reconstruction of ExNs (magenta) and inhibitory INs (white) shows 2.54-fold expansion of the IN pool from mouse to macaque and human, which (C) would predict a similar-fold increase in the inhibitory input onto ExNs, which would substantially alter the set point for the inhibitory versus excitatory synaptic input balance in human compared with mouse (illustrated for threefold increase). (D to F) Mapping of (D) the synaptic input to excitatory neuron dendrites showed (E) an unaltered rate of shaft input synapses but a 2.65-fold decrease of spine input synapses, resulting in (F) a 2.72-fold increase in the fraction of input synapses made onto dendritic shafts. (G) Other dendritic inputs were rare but slightly increased from mouse to macaque and human: doubly innervated spines,  $4.49 \pm 0.01$  versus  $4.68 \pm 0.01$  and  $6.91 \pm 0.01$ ; stub synapses,  $1.44 \pm 0.00$  versus  $2.17 \pm 0.01$  and  $4.71 \pm 0.01$ ; spine neck innervations,  $0.26 \pm 0.00$  versus  $0.84 \pm 0.00$  and  $0.67 \pm 0.00$ ;  $n = 1111, 598$ , and  $1040$  total synapses, respectively. [(F) and (G)] (Insets) EM images of example synapses from (F) human STG multiSEM-imaged and (G) (left to right) macaque STG, human IFG, and macaque S1, respectively.

(H) Concomitant increase of shaft synapse input could support the altered i/e balance model in (C), if axonal properties remain unchanged from mouse to macaque and human (analyzed in Figs. 3 and 4). Scale bars,  $1\text{ }\mu\text{m}$  unless indicated otherwise. Data in (A) are from automated reconstructions, and data in (B) and (D) to (H) are from expert reconstructions.

In the dense cortical neuropil, only a fraction of axons originates from neurons whose cell body is located in close proximity, whereas most have more distal origins. To study the target properties of all axons in the neuropil, also those without their cell body of origin in the dataset, we next analyzed the dense population of axons in mouse versus macaque and human that we obtained from the dense automated reconstructions ( $n = 202,954$  axons total with  $n = 1,618,129$  output synapses) (Fig. 3, D to F). Mouse axons predominantly innervated spines (Fig. 3E), as expected from the soma-based reconstructions (Fig. 3B) and the small fraction of INs (Fig. 2B). Densely sampled macaque and human axons, however, did

not reproduce the soma-based axonal properties but showed a broader distribution of spine innervation from 0 to 80% spine preference (here and in the following, spine preference implies fraction of an axon's synapses established as single spine innervations, not considering doubly innervated spines).

What could yield this difference in axonal properties between soma-based and dense reconstructions in macaque and human? In particular, we needed to understand the origin of axons with >40% spine targeting in macaque and human (Fig. 3E) that we had rarely observed in the soma-based reconstructions (Fig. 3B). Soma-based reconstructions in datasets smaller than the complete axonal arbor

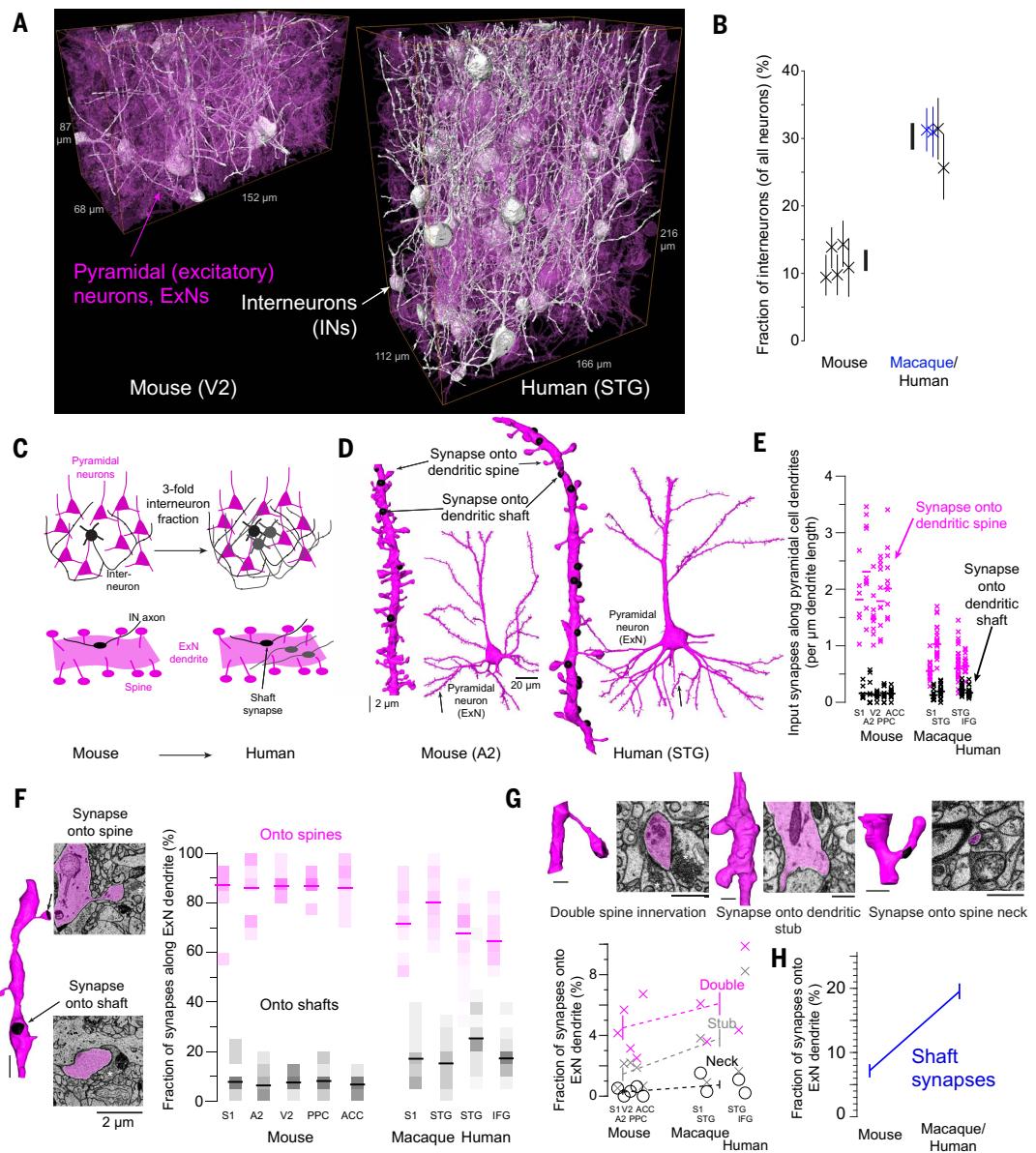


**Fig. 3. Synaptic target properties of excitatory and inhibitory neurons in mouse and human.** (A to C) Axonal target properties from identified pyramidal cells and INs ( $n = 50$  neurons,  $n = 2101$  output synapses, cross-validated expert reconstructions). All reconstructions are available at <https://wlink.org/7881> and <https://wlink.org/3103> (mouse), and <https://wlink.org/9448> and <https://wlink.org/2204> (human). (B) Absence of single spine innervation for INs in mouse and human, but shift in spine innervation of excitatory axons from mouse to human, yields a less separated synaptic preference of excitatory versus inhibitory axons. (D to F) Axonal target properties from dense axonal reconstructions in mouse, macaque, and human. Examples of dense axon populations from (D) mouse A2 and (F) human STG, all axons traversing boxes of 10 by 10 by 10  $\mu\text{m}$  size shown ( $n = 120$  and  $n = 89$ , respectively). Quantifications in (E) are based on all axons in the respective datasets ( $n = 202,954$  axons, with 5 to 25 output synapses each;  $n = 1,618,129$  synapses). Gray indicates distribution of spine target fraction for all axons in the datasets, uncorrected. Black lines indicate average likelihood function of true spine target fraction under consideration of error rates (Materials and methods).

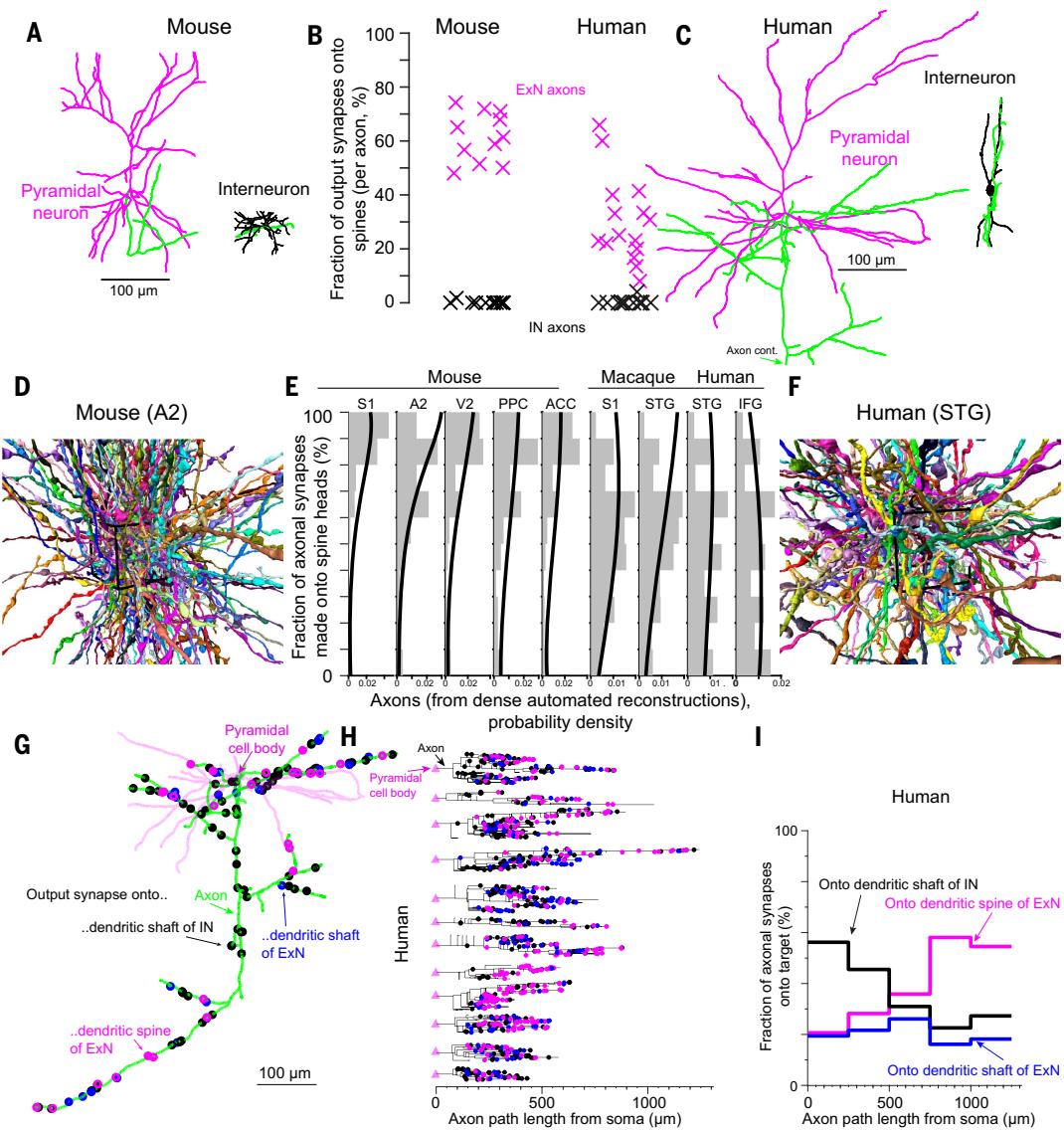
There is a broadening of axon target property distribution toward lower spine targeting in macaque and human compared with mouse that is, however, less pronounced than in (B) soma-based axon reconstructions. (G to I) Path length-dependent axonal synapse sorting (PLASS) as a possible origin of broader axonal target property distributions in human. (G) Example of pyramidal cell axon from human STG [path length, 3.74 mm,  $n = 132$  output synapses; same neuron as shown in (C)]. Colors indicate synaptic target of axonal output synapses. [(H) and (I)] Distribution of axonal output synapses along pyramidal cell axons from human STG ( $n = 15$  axons, 1126 output synapses, expert reconstructions,  $n = 12$  reconstructions from mSEM dataset shown). All axons from mSEM and SBEM datasets are available at <https://wlink.org/9448> and <https://wlink.org/2204>. Synapse symbols are as in (G). (I) Substantial increase in targeting of ExN spines over axonal path length. Data in (A) to (C) and (G) to (I) are from expert reconstructions, and data from (D) to (F) are from dense reconstructions.

#### Excitatory versus inhibitory synaptic input balance

We first identified synapses onto a dendritic shaft of distal pyramidal cell dendrites and reconstructed the presynaptic axon from these synapses (“shaft-seeded” axons). Then we determined these axons’ synaptic target properties on the basis of their other output synapses (Fig. 4A). Whereas in mouse, as expected, axons were clearly identifiable as excitatory versus inhibitory on the basis of their dichotomy in spine targeting preference (Fig. 4A), the distributions of axonal properties were much less distinct in human, recapitulating the properties of densely reconstructed axons in macaque

and human (Fig. 4A; compared with Fig. 3, B and E). Because this data did not allow the simple threshold-based classification of axons into inhibitory versus excitatory that can be used in mouse, we needed a more rigorous approach for axon type determination (Fig. 4, C to E).

We used the notion that the various types of axons and dendrites and their synaptic output and input properties in dense cortical neuropil are ultimately constrained by the synaptic composition of this neuropil volume (Fig. 4B). The volumetric density of synapses onto dendritic spines in the neuropil, for example,



has to be composed by the intermixing of the spine preference of the various axon types present in the neuropil and similarly for other types of synapses. Because dense 3D EM data allowed us to concomitantly measure the properties of extended stretches of axons and dendrites together with the dense volumetric synaptic composition of the neuropil, we could determine the occurrence and target properties of excitatory and inhibitory axons without having to make prior assumptions about their relative prevalence (Materials and methods).

We built a model in which the synaptic properties of excitatory and inhibitory axons

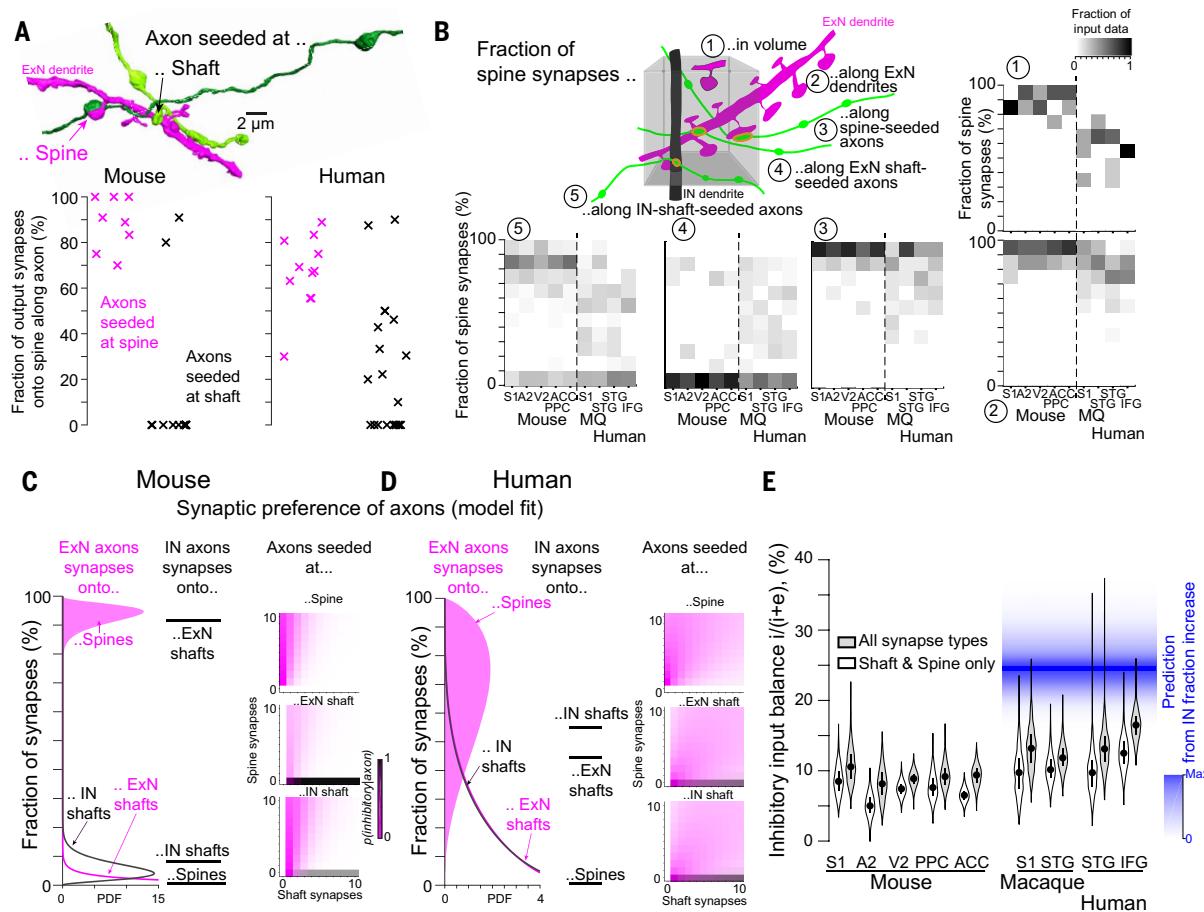


**Fig. 4. Detailed analysis of i/e balance onto ExN dendrites.** (A) Target properties of axons seeded at dendritic spines and shafts of ExN dendrites in mouse and human. (Top) Example reconstruction (macaque STG). (Bottom) Data from expert reconstructions in mouse S1 and human STG ( $n = 53$  axons,  $n = 626$  output synapses) showing shift of axonal targeting analogous to densely reconstructed axons in mouse versus human (compared with Fig. 3E). (B) Input data from expert annotations ( $n = 754$  axons,  $n = 11,308$  synapses total) that [(C) and (D)] fully constrain the model (Results and Materials and methods) (model validation is provided in fig. S2). Shaded magenta curve indicates distribution of spine targeting by ExN axons; magenta line indicates ExN shaft targeting by ExN axons;

and black line indicates IN shaft targeting by ExN axons. Shown is a broadening of ExN axons' spine targeting fraction and shift of excitatory and inhibitory shaft targeting from mouse to human. MQ, macaque. (E) Resulting estimates of inhibitory input fraction [ $i/(i+e)$ ] onto ExN dendrites in mouse, macaque, and human. Violin plots indicate expected inhibitory input synapse fraction along ExN dendrites (distribution across  $n = 1000$  bootstrap samples per dataset). Open shading indicates only shaft and single spine inputs considered; gray shading indicates that multiply innervated spines and other inputs are included (Fig. 2G). Synaptic input balance does not approach the inhibitory bias predicted by the increased fraction of INs in macaque and human. Blue shading indicates prediction from mouse to macaque and human ( $24.9 \pm 3.2\%$ , mean  $\pm$  SD;  $P < 0.001$ , by bootstrap sampling) (Materials and methods). All data are from expert reconstructions.

and their relative prevalence were determined (Fig. 4, C and D): Inhibitory axons were modeled with a multinomial distribution based on point estimates for their synaptic target preferences, whereas for excitatory axons, a distribution of target preference was modeled with a Dirichlet-multinomial to account for the effects of broadened synaptic preference shown in Fig. 3 (Materials and methods). The model was fully constrained by the following input data, which we obtained from carefully curated expert reconstructions in all datasets ( $n = 11,308$  synapses annotated) (Fig. 4B): (i) volumetric fraction of spine synapses, (ii) fraction of input synapses onto spines along

spiny (ExN) dendrites, (iii) fraction of output synapses onto spines along axons seeded from ExN dendritic spines, (iv) fraction of output synapses onto spines along axons seeded from ExN dendritic shafts, and (v) fraction of output synapses onto spines along axons seeded from IN (smooth) dendritic shafts. These input data did not require a pre hoc classification of the synapses or axons as inhibitory versus excitatory and did not contain the axons reconstructed from identified cell bodies (Fig. 3, A to C). With this input data, we obtained fits of the synaptic target properties of excitatory and inhibitory axons in each dataset (Fig. 4, C and D, shown for mouse S1 and human

STG datasets): point estimates for the fraction of synapses made onto ExN spines, ExN shafts, and IN shafts for inhibitory axons (Fig. 4, C and D) and distributions of these target fractions for excitatory axons. Together with the modeled relative prevalence of inhibitory versus excitatory synapses, for any axonal stretch with any combination of  $x$  synapses onto shaft and  $y$  synapses onto spine, we obtained a probability of this axon to be excitatory versus inhibitory (Fig. 4, C and D, right). For validation of the model, we used the soma-based axon reconstructions (Fig. 3, A to C) for which we had certainty about their excitatory versus inhibitory property, sampled local stretches

from these ground truth axons, and asked the model to predict their excitatory versus inhibitory character (E→I and I→E misclassification rates: 0 and 0% for mouse, 6.9 and 8.4% for primates, respectively) (fig. S2 and supplementary materials, materials and methods).

We then applied the model to determine the expected inhibitory versus excitatory synaptic properties of ExN dendrites in all datasets (bootstrapped to account for sample size in input data and controlled for initial conditions; Materials and methods) (Fig. 4E). We found that the inhibitory input balance increased only moderately from  $9.3 \pm 0.8\%$  (mean  $\pm$  SD) in mouse to  $13.8 \pm 1.4\%$  ( $P = 0.001$ , bootstrap sampling) in macaque and human, revoking a setting in which the inhibitory-to-excitatory input balance were to change in proportion to the 2.5-fold increase in IN fraction from mouse to macaque and human (Fig. 4E; compared with Fig. 3C) ( $P = 0.003$ ; when also considering all other types of input synapses,  $P < 0.001$ ; bootstrap sampling; Materials and methods). Rather, the increased fraction of shaft input synapses coincided with a change in axonal targeting properties: Excitatory axons made  $0.7 \pm 0.3\%$  of their synapses onto ExN shafts in mouse, but  $12.0 \pm 1.1\%$  in macaque and human ( $P < 0.001$ , bootstrap), and their IN shaft targeting changed from  $4.4 \pm 0.7\%$  to  $17.3 \pm 1.7\%$  ( $P < 0.001$ , bootstrap), which is consistent with the automated axon reconstructions.

This lack of enhanced inhibition onto ExN dendrites was also found for the proximal input domains of pyramidal cells [axon initial segment (AIS), soma, and proximal dendrites] (fig. S1), excluding the possibility that inhibitory synapses had been redistributed toward the perisomatic domains.

These data yielded the question of where the expanded inhibitory population in human is establishing its synapses.

#### **Properties of the expanded inhibitory neuronal network in human**

To determine the inhibitory network properties in mouse versus human, we first applied a simple IN classification based on the configuration of IN dendrites as multipolar (MP) versus non-MP [which included bipolar, bitufted, and vertically oriented dendritic trees (Fig. 5, A to D), labeled as “bipolar” (BP) for simplicity]. The IN pool changed from dominated by MP INs in mouse (about 70 to 82% MP versus 18 to 30% BP,  $n = 52$  versus 17) (Fig. 5D) to a majority of BP INs in macaque and human (53% BP;  $n = 122$  MP versus  $n = 135$  BP,  $P < 0.01$ ; a test is described in Materials and methods) (Fig. 5D). When mapping the synaptic target properties of these classes of INs in mouse versus human (Fig. 5, E and F), we found a fraction of BP INs with almost exclusive innervation of other INs in human that was not found in mouse. IN targeting by BP IN

axons increased from 56% (Fig. 5, F and G) (70 IN targets out of 126 synapses,  $n = 4$  axons) to 72% (Fig. 5G) (225 IN targets out of 314 synapses,  $n = 9$  axons,  $P = 0.018$ ) (Materials and methods) (63). The changed IN pool composition together with the changed distribution of IN targeting properties would predict a substantial increase of IN-preferring inhibitory axons in the dense neuropil of human versus mouse (Fig. 5F). When analyzing the target preferences of inhibitory axons for smooth (IN) dendrites in mouse versus macaque and human from the dense automated reconstructions (Fig. 5H), we found a substantial shift toward IN-to-IN connectivity that can account for the inhibitory synapses contributed by the expanded IN pool in macaque and human (average smooth dendrite targeting probability of inhibitory axons,  $8.0 \pm 15.0\%$  in mouse versus  $21.4 \pm 29.0\%$  in human;  $n = 6565$  versus  $n = 2048$  axons;  $P = 2.2 \times 10^{-104}$ , one-sided KS test). Together with the increased IN fraction (Fig. 2B), this would estimate the IN-to-IN network to expand 6.7-fold from mouse to human. On the basis of the model (Fig. 4), we estimated the expansion to be 8.6-fold (from  $1.0 \pm 0.2\%$  IN-IN connectivity in mouse to  $8.6 \pm 1.4\%$  in macaque and human) (fig. S2F and supplementary materials, materials and methods).

To better understand the contributions of types of INs to this enhanced network, we then analyzed the synaptic input balance onto IN dendrites in MP and BP INs in mouse, macaque, and human (Fig. 5, I to K). To our surprise, already in mouse, MP INs and BP INs have different inhibitory input balance (Fig. 5, I and K): Whereas MP INs receive  $7.6 \pm 2.5\%$  inhibitory input (bootstrapped mean  $\pm$  SD;  $n = 105$  axons from  $n = 5$  mouse datasets,  $n = 977$  synapses total), BP INs receive  $26.2 \pm 5.0\%$  ( $n = 88$  axons,  $n = 694$  synapses,  $P = 0.001$ ). In macaque and human, MP INs receive inhibitory input that is commensurate to the fraction of INs in the cortex ( $24.2 \pm 6.4\%$ ,  $n = 69$  axons from  $n = 4$  datasets,  $n = 514$  synapses;  $P = 0.6$  for scaling by IN fraction increase), whereas BP INs receive further enhanced inhibition ( $44.3 \pm 7.8\%$ ,  $n = 71$  axons,  $n = 506$  synapses,  $P = 0.026$ ). These data indicate differential inhibitory targeting across species and may imply separate IN-to-IN circuits to be substantially enhanced in macaque and human.

#### **Excitatory synaptic network**

Last, we wanted to determine the magnitude of the synaptic input to pyramidal cells in human cortex. With the expanded size of pyramidal cell dendritic trees, it has been assumed that human pyramidal cells receive a larger number of input synapses than that of mouse pyramidal cells (from about 10,000 to about 30,000) (15, 29, 43, 44, 46). Because we found a strongly reduced spine-targeting synapse den-

sity in the human cortex (Fig. 2E), we wondered what the quantitative input structure of human pyramidal cells would be (Fig. 6, A and B, and figs. S1 and S4).

We used our large-scale 3D EM datasets obtained in one human individual that spanned the entire depth of cortical gray matter to reconstruct a substantial portion of L2/3 pyramidal cells. On the basis of these reconstructions, we extrapolated to the full extent of the dendritic tree. The large dataset extent in-plane allowed us to map some pyramidal cell dendrites in their full extent from soma to dendritic tip and to use the properties of these completely mapped dendrites for estimating the total path length of pyramidal cell dendrites in human (Materials and methods). The resulting estimates of total dendritic path length (about 9 to 20 mm path length) (Fig. 6B and fig. S4) were consistent with light-microscopic reconstructions (43, 45). Because we measured synaptic input density in parallel, we could exclude a compensation of lower dendritic path length by higher spine-targeting synapse density for individual pyramidal cells. Together, total synaptic input to pyramidal cells was 12,000 to 17,000 in human L2/3, which is far below an increase corresponding to the about threefold thicker cerebral cortex yielding about threefold larger pyramidal cell dendritic trees compared with those of mouse (Fig. 6B).

#### **Discussion**

The comparative analysis of mouse, macaque, and human cortical neuronal networks revealed that the most substantial changes in neuronal architecture—the increase of pyramidal cell size and the numeric expansion of the IN pool—have not resulted in the most immediate possible circuit changes: neither an increase of total synaptic input on pyramidal cells nor an overall shift of their synaptic input balance toward inhibition. Rather, we found an at least six- to eightfold expanded IN-to-IN network in the macaque and human cortex (Fig. 6C and fig. S2F). These circuit alterations point toward IN-to-IN connectivity as a key evolutionary change from mouse to primates, including human.

#### **Dependence of spine densities on age**

Our finding of an almost constant total synaptic input to human pyramidal cells when compared with those of mouse may be affected by a reported age-dependent decline of dendritic spines in cortex (70–72), which could amount to a reduction in spine density of 45 to 48% during puberty (72). The human samples were from individuals in the upper quarter of expected life length. However, we found low spine densities in macaque as well, at about 50% life expectancy. Similarly, rodents of 50 to 80% life expectancy show spine densities comparable with those reported here for younger mice (55, 67). It is therefore unlikely that

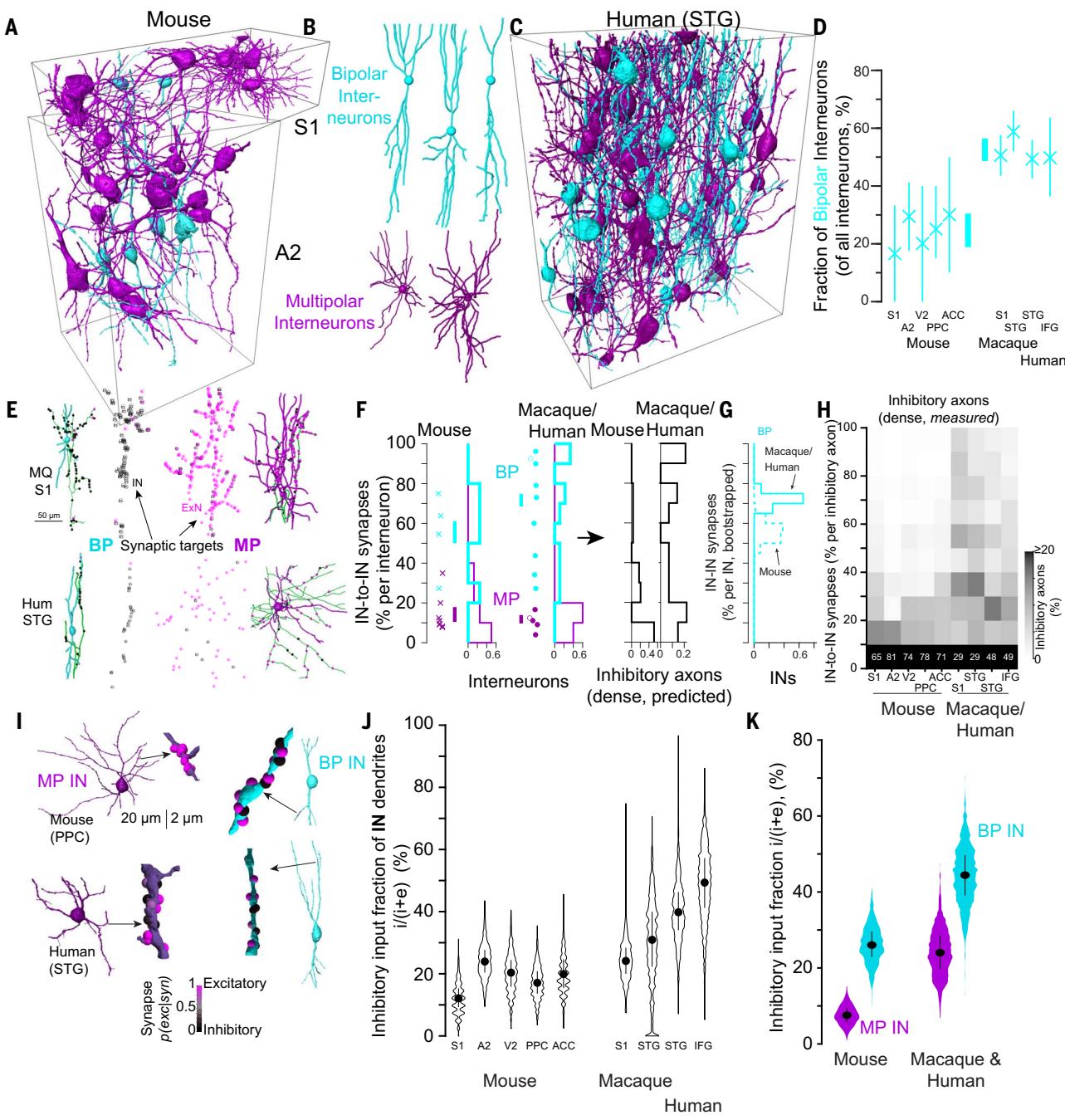
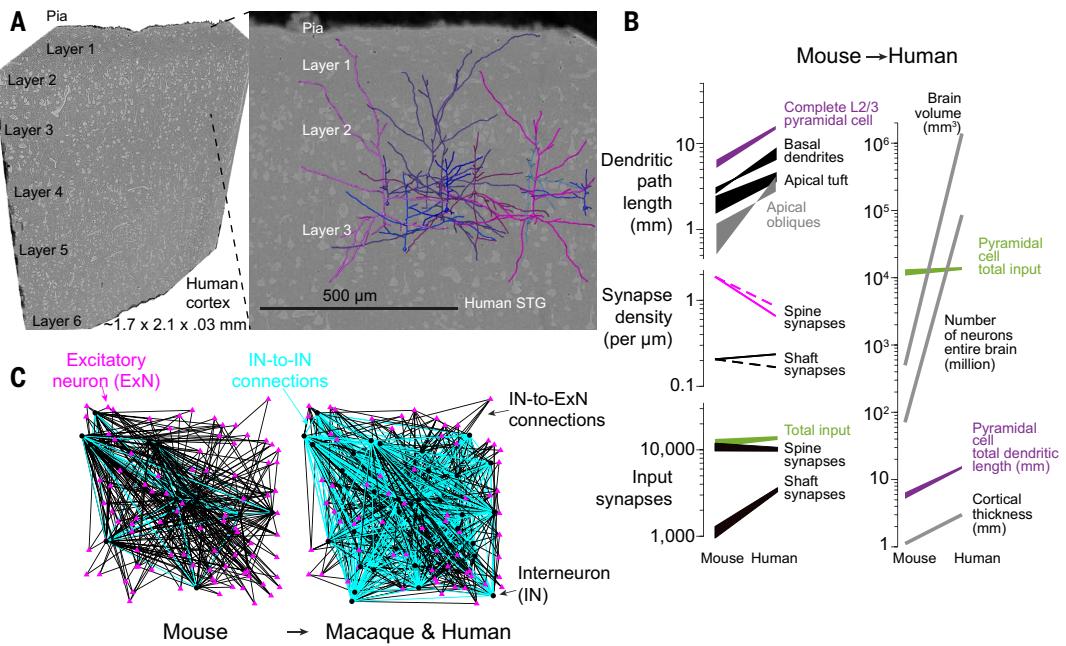


**Fig. 5. Selective expansion of IN types and its effect on the inhibitory-to-inhibitory network.** (A to C) Dense reconstruction of all INs in (A) mouse and (C) human with (B) labeling of MP (purple) versus BP (cyan) INs showing sparsity of BP INs in (A) mouse compared with (C) human. (D) Proportion of BP INs 2.3-fold expanded from mouse to macaque and human. (E) Synaptic targets of BP versus MP INs in macaque and human show selectivity for (left) inhibitory (93% of synaptic targets) versus (right) excitatory (87% of synaptic targets) postsynaptic partners. (F) Broader distribution of IN innervation selectivity in macaque and human versus mouse from soma-based axon reconstructions. This predicts expansion of inhibitory-to-inhibitory connectivity in macaque and human versus mouse (right). (G) Within the BP INs, IN targeting is further enhanced (from  $56.63 \pm 4.46\%$  to  $71.67 \pm 2.48\%$ ;  $P < 0.05$ , bootstrapped from 126 and 314 synapses, respectively, for mouse versus macaque and human). (H) Analysis of densely reconstructed inhibitory axons and their targeting

of IN dendrites ( $n = 94,391$  synapses,  $n = 11,384$  axons) by inference of the most likely smooth dendrite targeting probability under consideration of the error rates of automated synapse detection. (F) Expansion of IN-to-IN connectivity as predicted from soma-based reconstructions. (I to K) Detailed analysis of inhibitory input balance to MP versus BP IN subtypes across species. (I) Example reconstructions of input synapses onto IN dendrites. (J) Inhibitory input determined from the model in Fig. 4 for IN dendrites. The 2.35-fold increase from mouse to human ( $18.9 \pm 2.5\%$  to  $44.5 \pm 7.3\%$ , mean  $\pm$  SD) is consistent with the prediction from IN expansion for IN dendrites ( $P = 0.662$ ). [(J) and (K)] Separate analysis of inhibitory input to MP versus BP INs reveals a difference in inhibitory input already in mouse (7.6 versus 26.2%;  $P = 0.001$ ) that is further enhanced in macaque and human (24.2 versus 44.3%;  $P = 0.026$ ). Data in (H) are from dense reconstructions; all other data are from expert reconstructions.

**Fig. 6. Scaling of pyramidal cell synaptic input and network properties from mouse to human.** (A) Large-scale 3D EM dataset spanning all cortical layers from human cortex (STG) for reconstruction of dendritic arbors of L2/3 pyramidal neurons. (B) With about threefold reduced spine density from mouse to human, the about threefold increase in pyramidal cell dendritic path length yields only moderately increased number of input synapses for human pyramidal cells compared with that in mouse. Dashed lines indicate macaque. (C) Expanded IN-to-IN network, illustrated according to model fit (Fig. 4; fig. S2F; and supplementary materials, materials and methods). There is an 8.6-fold expansion of IN-to-IN connectivity from mouse to macaque and human. Data in (A) and (B) are from expert reconstructions. In (B), right, lower limits of pyramidal cell total dendritic length and total input are based on (45); upper limits are based on data in this study. Brain volume is based on (101), and the number of neurons in the entire brain is based on (1).



age-related effects have dominated the finding of reduced spine densities in human compared with mouse. Also, although temperature-dependent changes in spine densities have been reported (73), these are unlikely the cause of our measured spine densities (Fig. 2E and supplementary materials) (29, 44, 46, 55, 66, 74–77).

#### Synaptic strength versus synaptic number

Our data indicate the maintenance of the relative number of inhibitory versus excitatory input synapses on the dendrites of pyramidal cells in human versus mouse. The effective balance between inhibition and excitation could be altered by different strengths of synapses. Evidence for larger unitary excitatory postsynaptic potentials and for larger synapses and presynaptic vesicle pools has been found in experiments on human cortical slices (16, 30, 78, 79). At the same time, the impact of single inhibitory synapses is enhanced (19, 20). Whether synaptic number is a proper indicator of overall synaptic impact is a matter of investigation, with evidence in ferret (80) pointing toward a dominant effect of synapse number, as we quantified in this work.

#### Increased complexity of inhibitory networks

The IN-to-IN network expansion found in macaque and human could have a multitude of dynamic effects. Although the most immediate consequence could be a more evolved disinhibitory network capability—for example, for the gating of otherwise inhibited excitatory activity (81, 82)—theoretical studies have also indicated possible effects on the maintenance

of working memory through enhanced IN-to-IN connectivity and the ensuing network dynamics (83). Our data indicate that a detailed investigation of such phenomena is required for an understanding of the human cortex. In particular, alterations in IN-to-IN connectivity should become a focus of study in the context of possible pathological alterations of human cortex.

#### Materials and methods

##### Animal experiments and human tissue samples

All animal-related experimental procedures were performed according to the law of animal experimentation issued by the German Federal Government under the supervision of local ethics committees and according to the guidelines of the Max Planck Society. Experimental procedures were approved by Regierungspräsidium Darmstadt, AZ: F 126/1002 (mouse) and Regierungspräsidium Marburg AZ: V54 -19c 20 15 hours 01 MR 13/1 Nr. 78/2012 (macaque).

The human brain tissue samples were collected during neurosurgical procedures that were indicated for medical reasons and independently from this research project at the Department of Neurosurgery at the Klinikum rechts der Isar of the Technical University of Munich. They were obtained from access tissue (presumably healthy brain parenchyma that had to be removed as part of the procedure and would have been discarded otherwise) before removal of the respective target lesions, as approved by the Ethics Committee of the Technical University of Munich School of Medicine (Ethikvotum 184/16S and 273/21 S-EB).

All patients had given their written informed consent.

The macaque brain tissue sample was collected at German Primate Center (DPZ) GmbH, Göttingen.

#### Tissue extraction and preparation

Mouse tissue was processed and imaged as described previously (49, 55, 84). These consisted of four 3D-EM datasets from layers 2/3 of mouse S1, V2, PPC and ACC sized between 72 by 93 by 141  $\mu\text{m}$  and 88 by 56 by 213  $\mu\text{m}$  (Fig. 1) acquired at a voxel size of 11.24 to 12 by 11.24 to 12 by 28 to 30 nm the present study densely reconstructed and reanalyzed these published datasets from mouse, together with a newly acquired dataset from mouse A2 cortex. The published mouse dataset “PPC-2” (55) covering layers 1 to 5 was also used for expert reconstructions.

The human and macaque samples were processed as follows. All tissue specimen were fixed by either immersion (human) or transcardial perfusion (macaque) using an EM fixative composed of 2.5% paraformaldehyde (Sigma), 1.25% glutaraldehyde (Serva) and 2 mM calcium chloride (Sigma) in 80 mM cacodylate buffer adjusted to pH 7.4 with an osmolarity ranging from 700 to 800 mOsmol/kg (85).

The human “H5” tissue was obtained from the right superior temporal gyrus of an 80 year old male patient during resection of a temporal mass lesion (final diagnosis: glioblastoma multiforme). After removal the sample was immersed in cold (13°C) EM fixative and transported to a nearby laboratory (transport time

about 6 min). Partially submerged in cold fixative the sample was manually trimmed along the pia-WM axis and mounted on a vibratome stage. Then, submerged in cold EM fixative, the sample was cut into 500  $\mu\text{m}$  thick slices with a vibratome (Leica VT 1200S). The slices were then transported in 8 to 12°C cooled fixative and stored over night at 4°C. The next day, samples spanning the entire cortical depth and about 1.5 to 1.7 mm in width were cut out and prepared for electron microscopy as described in (55) with the modification that the sample was embedded in Epon Hard for sectioning in the ATUM. For this, samples were infiltrated through a graded series (3:1 for 4 hours, 1:1 12h/overnight, 1:3 for 4 hours) of aceton and Epon resin (Epon hard mixture: 5.9 g Epoxy, 2.25 g DDSA, 3.7 g NMA, 205  $\mu\text{l}$  DMP; Sigma-Aldrich). Samples were then incubated in pure resin for 4 hours at room temperature, 12 hours/overnight at 4°, and another 4 to 5 hours at room temperature. Samples were directly embedded in pure resin on aluminum pins and kept in a pre-warmed oven (60°) for 2 to 3 days. Fresh resin was prepared for each incubation step.

The cured sample was trimmed into a hexagonal shape (size 3.1 by 1.8 mm) with a diamond milling head using an EM trimmer (Leica EM TRIM2, Leica Microsystems, Wetzlar, Germany). Next, the sample was cut into 35- to 40-nm-thick slices at 0.3 mm  $\text{s}^{-1}$  cutting speed using a 4 mm ultra35° knife (DiATOME, Nidau, Switzerland). The ultrathin sections were collected on plasma-treated, carbon coated Kapton tape (custom-processed) with a customized ATUM-tome (RMC Boeckeler, Tucson, USA) (51, 52). The tape was then mounted on silicon wafers using double-sided adhesive carbon tape (P77819-25, Science Services GmbH, Munich, Germany). In total, 7009 slices (corresponding to an extent of 270.25  $\mu\text{m}$ ) were cut.

The human "H6" sample was obtained from inferior frontal gyrus from a 69 year old female patient during surgical removal of frontal mass lesion (final diagnosis: glioblastoma multiforme). Following surgical removal, tissue was directly collected in fix solution kept at 4°C. The tissue was immediately sliced into 500  $\mu\text{m}$  thin slices in cold fixative using vibratome. Slices were kept at 4°C overnight. Samples were then collected using 1mm circular medical biopsy punch (covering L2/3) and prepared for SBEM as described in (55).

The macaque sample was acquired from a 15.6 year old right handed male animal. Transcardial perfusion was performed under anesthesia (Ketamin, Xylazin) after an additional lethal dose of Barbituate (90 to 120 mg/kg intravenously). After flushing with ~2 l of 0.15 M cacodylate buffer (pH 7.4, duration 15 min) the perfusion solution was changed to ~2 l of EM fixative. The brain was removed and the anterior half of the brain was sectioned into 5-mm-thick

coronal sections. The sections were subsequently immersed in cold EM fixative, transported to the research laboratory and kept at 4°C over night. Within 48 hours the tissue was further dissected (with storage in 4°C EM fixative between processing steps). A ~5 mm wide tissue block centered on the anatomically defined arm/finger region of the left postcentral gyrus (Area 3a/b) medially adjacent to the rostral end of the intraparietal sulcus was dissected. The block was placed in 0.15 M cacodylate buffer and cut along the medio-lateral axis into 600  $\mu\text{m}$  thick slices using a vibratome (Microm HM650V, Thermo Scientific). Using a medical biopsy punch (KAI medicals, USA), a 1.5-mm-wide sample spanning almost the entire thickness of the cortex was cut and subsequently prepared according to the methods described in (55) using an automated tissue processor (Leica EM AMW).

### 3D EM imaging and image alignment

SBEM datasets of the human (H5, H6), macaque and mouse (A2) samples were acquired using a custom-built SBEM microtome [(50) courtesy of W. Denk] mounted inside the chamber of a scanning electron microscope (FEI Verios, Thermo Fisher Scientific, USA). The image acquisition and SBEM microtome were controlled using custom written software (55). Focus and stigmatism were adjusted using custom written auto-correction routines. Imaging parameters were as follows: 4 by 6 (macaque, H5, H6) or 3 by 4 (mouse A2) mosaic tiles of images sized 4096 by 3536 voxels with an in-plane voxel size of (11.24 nm)<sup>2</sup> and 30 nm nominal cutting thickness at 400 ns (macaque) or 700 ns (H5, H6, A2) dwell time with a nominal beam current of 800 pA (macaque) or 400 pA (H5, H6, A2).

Two multi-SEM datasets of sample H5 were acquired as follows. In one experiment, 767 slices (476 at 35 nm, 291 at 40 nm) were imaged with a 61-beam multiSEM (multiSEM 505, Carl Zeiss Microscopy GmbH, Oberkochen, Germany) at a landing energy of 1.5 kV, a pixel size of 4 nm and a pixel dwell time of 50 ns with an FOV per slice of 1.7 by 2.1 mm. In a second experiment (H5\_ext), 1342 additional slices (thickness 35 to 40 nm, corresponding to about 54  $\mu\text{m}$  extent) were imaged with a smaller FOV per slice (1.1 by 1.1 mm) and aligned together with the previous experiment resulting in a total of 82  $\mu\text{m}$  depth.

Image alignment for SBEM datasets was performed using global 3D relaxation of shift vectors calculated by SURF feature detection as in (86) followed by subimage alignment as in (49). The aligned image volume was then saved in the webKnossos (87) three-dimensional image format. Human H5 (STG), H6 (IFG), macaque (STG), and mouse (A2) SBEM datasets were aligned by scalable minds, Postdam (supplementary materials, materials and methods) (88).

Image alignment for the two multiSEM datasets from sample H5 were performed similar to (55), following the alignment routines in (89) and [https://github.com/billkarsh/Alignment\\_Projects](https://github.com/billkarsh/Alignment_Projects), with modifications.

### Cell type classification

For analyses in Fig. 2, A and B, cell bodies were manually annotated by an expert annotator in webKnossos (87). All cell bodies were identified and classified into pyramidal cell, IN and glia. Pyramidal cells were identified based on presence of an apical dendrite directed toward the pia, an AIS directed toward the white matter, and spiny dendrites. INs were identified based on their large somata, which contained large numbers of mitochondria, an axon often exiting from a dendrite, lack of a clear apical dendrite or, if presence of an apical-like dendrite, lack of basal dendrites and WM-directed AIS, and smooth dendrites. Non-neuronal cells were distinguished primarily by their smaller cell bodies and different nuclear shapes.

For distinction of MP versus BP INs (Fig. 5, A to D), the dendrites of all identified INs were reconstructed and inspected in the coronal and tangential plane (90–98). INs with short dendritic lengths were excluded from this classification.

### Dendrite reconstructions

Pyramidal and IN dendrites (Fig. 2, D to G) were reconstructed by an expert annotator by following their trajectory throughout the dataset volume and placing nodes as described previously in (55, 84). From these dendrites for which the identity of the originating cell body had been determined, a distal stretch of 3 to 49  $\mu\text{m}$  length (mouse) and 7 to 44  $\mu\text{m}$  length (macaque and human) was used for annotation of all input synapses.

### Annotation of input synapses on dendrite, soma, AISs

Analyses reported in Fig. 2, D to G, and fig. S1 were conducted as follows. For a given postsynaptic target class (dendrites, somata, or AIS), all input synapses were identified based on the presence of a presynaptic vesicle cloud and postsynaptic density [as described in (55, 67, 84); see following section]. These synapses were labeled as single spine when only one presynaptic bouton was found for a dendritic spine; double spine when two input synapses were found for which a clear distinction into primary (excitatory) and secondary (inhibitory) was not possible; primary spine and secondary spine when two input synapses were found for which this distinction was possible; neck for spine neck innervations, stubby spine synapses when a short dendritic protrusion of larger diameter than a spine neck and without clear diameter change at the end (no clear spine head) was synaptically innervated, and shaft

synapses when the synapse was clearly placed on the main dendritic process without noticeable protrusion. Distances of synapses from the soma were measured using minimum spanning tree on the annotated nodes of the dendrites (see “skeleton” class in code repository).

#### Soma based axon reconstructions

Analyses reported in Figs. 3, A to C and G to I, and 5, E and F, were conducted as follows. The axons of identified pyramidal cell and INs were reconstructed by first identifying the exit at the AIS. Then the trajectory of the axon was followed throughout the dataset and comments were added at the outgoing synapses. The post-target of each synapse was further classified into excitatory or inhibitory class based on their spine-targeting synapse density (when target was dendritic) or cell body type (when target was a soma or an AIS). Axons with fewer than 10 synapses were excluded to allow higher signal-to-noise ratio per axon.

#### Synapse-seeded axon reconstructions

Analyses reported in Fig. 4, A and B, were conducted as follows. For a given postsynaptic target with identified input synapses, a skeleton node was placed in the presynaptic axon’s vesicle cloud and commented as “seed” synapse. The presynaptic axon was then reconstructed throughout the entire dataset volume, and all of the axons’ other output synapses and their corresponding postsynaptic targets were identified as described in the following section. The “seed” synapse was excluded when quantifying axonal spine target properties in Fig. 4A.

#### Synapse identification for reconstructed axons

For analyses reported in Figs. 3, A to C and G to I; 4, A and B; and 5, E and F, the following synapse identification was applied. For each reconstructed axon, synapses were identified manually when following the trajectory of axon. First, vesicle clouds in the axon were identified as accumulations of vesicles. Subsequently, the most likely postsynaptic target was identified by the following criteria: direct apposition with vesicle cloud; presence of a darkening and slight broadening of the synaptic membrane; vesicles at close proximity to the plasma membrane at the site of potential synaptic contact. Synapses were marked as uncertain whenever the signs of darkened postsynaptic density could not be clearly identified. All analysis in this study were conducted only on synapses that had been classified as certain. For each axon, at every subsequent synapse location, a node was placed in the vesicle cloud and commented with the corresponding postsynaptic target’s identity (for example, soma, AIS, dendritic shaft, dendritic single spine, dendritic double-innervated spine, spine neck, stub, somatic spines or filopodium). All synapses were annotated by

an expert annotator; for unclear cases, these were re-annotated for expert consensus between two or three experts.

#### Volumetric model of synapse and axon types, inference of synapse and axon types, automated reconstruction, and error analysis

These methods are reported in the supplementary materials.

#### Estimates of total dendritic path length of human pyramidal cells

For the estimation of the complete synaptic input onto a L2/3 pyramidal cell (Fig. 6, A and B, and fig. S4), all dendrites of 10 L2/3 pyramidal cells were reconstructed until their end in dataset H5, which was either the actual ending of the dendrite in the neuropil, or the end of the dendrite at the dataset boundary (Fig. 6A). In addition, nine pyramidal cells in the extended dataset H5\_ext were analyzed with a larger fraction of in-dataset dendrite endings. Results from both datasets yielded similar ranges for total dendritic path length estimates, as detailed in the following.

For the following calculations, only dendrites with actual in-dataset endings were used (one exception were apical tuft dendrites in which some dendrites without in-dataset endings had more branch points and were therefore included in the estimate). This approach could correspond to an underestimation of dendrite length; therefore, in addition to the length measurements described here, we also used length reports from light-microscopically imaged human L3 pyramidal neurons, which provided similar path length measurements (ranges in Fig. 6B) (45).

For each pyramidal cell, the following dendritic compartments were distinguished: (i) apical dendrite trunk (measured from the exit at the cell body toward pia along the cortical axis, until the main bifurcation), (ii) apical tuft (measured from the main bifurcation point of the apical dendrite), (iii) oblique dendrites (measured from the exit at the apical dendrite trunk), and (iv) basal dendrites (all dendrites exiting at the cell body except the apical dendrite) (55).

For the basal, oblique and apical tuft compartment  $n = 226, 211$ , and  $167$  dendrites were reconstructed of which  $n = 25, 28$ , and  $32$  dendrites with in-dataset endings were found ( $n = 21$  cells).

For the estimation of the average number of branch points for the apical tuft compartment dendrites without in-dataset endings were included to avoid an underestimation of dendrite length as some of them had more branch points than the dendrites with in-dataset endings. For this, all apical tuft dendrites beyond a  $300\text{-}\mu\text{m}$  threshold were included ( $n = 64$  dendrites, with  $n = 32$  in-dataset endings,  $n = 21$  cells).

The estimations for the lengths of the above compartments were done as follows. The length for apical dendrite trunk compartment was estimated by averaging the lengths over all the samples from their soma exit until the main bifurcation. For each of the remaining compartments (i.e., apical tufts, oblique and basal dendrites), the path lengths (PLs) between consecutive branch points (BPs) were measured until a true end was reached. The order of a branch point (“order”) was defined as the number of edges along the unique path between it and the cell body node (for example, order is 0 at the cell body node, 1 at first branch point, 2 at second branch point and so on). Then for the entire compartment (apical tuft, oblique or a basal dendrite), the total length was calculated by summing the path lengths of each segment times 2 to the power order of the corresponding branch point:  $\sum_{\text{order}=0}^{\text{BP}} PL_{\text{seg}, \text{order}} * 2^{\text{order}}$  where order = order of a branch point, BP = mean number of branch points for each compartment and  $PL_{\text{seg}, \text{order}}$  = path length of the succeeding segment at the corresponding branch point order. Then, the resulting total length of each compartment was multiplied with the average number of basal, oblique or apical tuft exits to estimate lengths for all basal, oblique and apical tufts respectively. The model of the branching as binary to the final branch point order would likely overestimate total dendritic path length, thus not affecting the conclusion about low total input synapse numbers in human.

To estimate the number of input synapses for each of the dendritic compartments, we proceeded as follows. For each compartment (apical trunk, apical tuft, oblique or basal dendrite), dendritic segments of path length  $10$  to  $50\text{ }\mu\text{m}$  were sampled and all input synapses were annotated. For computing the spine-targeting synapse density per dendritic shaft path length, both single spine head and primary spine head synapses were included. For shaft synapse density, only the shaft synapses were included. For total synapse density, additionally secondary spine head, spine neck and dendrite “stub” synapses were included (total fraction of these additional synapses: less than 10%). The average spine, shaft and total synapse densities were then multiplied with the total path lengths of the corresponding compartments. The apical dendrite trunk was additionally distinguished into a proximal segment (up to  $50\text{ }\mu\text{m}$  from cell body) and a distal segment ( $50\text{ }\mu\text{m}$  from soma until the main bifurcation). Similarly, the basal dendrites were additionally distinguished into a proximal segment which showed high shaft synapse density (up to  $30\text{ }\mu\text{m}$  from cell body for mouse,  $80\text{ }\mu\text{m}$  for human).

For the basal compartment we measured spine-targeting and shaft synapse densities of  $0.66 \pm 0.23$  per micrometer and  $0.23 \pm$

0.09 per micrometer ( $n = 13$ ), for the oblique compartment  $0.67 \pm 0.23$  per micrometer and  $0.19 \pm 0.06$  per micrometer ( $n = 14$ ), for the apical tuft compartment  $0.73 \pm 0.34$  per micrometer ( $n = 12$ ) and  $0.25 \pm 0.07$  per micrometer ( $n = 12$ ), respectively.

For the proximal segment of the apical trunk we measured spine-targeting and shaft synapse densities of  $0.06 \pm 0.14$  per micrometer and  $0.44 \pm 0.16$  per micrometer ( $n = 9$ ), for the distal segment until the main bifurcation  $0.45 \pm 0.39$  per micrometer and  $0.20 \pm 0.08$  per micrometer ( $n = 7$ ), respectively.

### Statistical tests

All statistical tests were KS for fractions and ratios, and Wilcoxon ranksum tests, otherwise. Data are shown as box or violin plots with median, 25th and 75th percentile and outliers (using MATLAB, Mathworks). All tests are documented in the code repository (next section).

The test of significance for increase in IN fraction from mouse to macaque/human was done by pooling all identified excitatory neurons and INs counts per species group and generating 1000 bootstrap samples (99) with replacement. IN fraction ( $\text{IN}_{\text{frac}}$ ) was computed for each bootstrap sample. The  $P$ -value was calculated as the fraction of bootstrap samples in mouse for which  $\text{IN}_{\text{frac}}$  was greater than or equal to the lowest  $\text{IN}_{\text{frac}}$  in macaque/human bootstrap group (Fig. 2B, error bars 10th to 90th percentiles). The same bootstrap approach was used as a test of significance for increase in non-MP IN fraction from mouse to macaque/human by pooling all MP and non-MP INs in volume per species group (Fig. 5D, error bars 10th-90th percentiles) and similarly for testing increase of IN-targeting fraction of non-MP IN axons from mouse to macaque/human by pooling all output synapses of non-MP IN axons per species group (Fig. 5, F and G).

### Data availability

All electron microscopy datasets are publicly available for browsing at webknossos.org: macaque L2/3 (S1), <https://wklink.org/1186>; macaque L2/3 (STG), <https://wklink.org/1319>; human (H5) L23 (STG), <https://wklink.org/7861>; human (H5) L23 (STG) multiSEM, <https://wklink.org/5364>; human (H5) L1-6 (STG) multiSEM, <https://wklink.org/1742>; human (H6) L2/3 (IFG), <https://wklink.org/7299>; mouse L2/3 (S1), <https://wklink.org/9045>; mouse L2/3 (PPC), <https://wklink.org/2581>; mouse L2 (ACC), <https://wklink.org/7415>; mouse L2/3 (V2), <https://wklink.org/3592>; mouse L2/3 (A2), <https://wklink.org/7193>; mouse L1-5 (PPC-2), <https://wklink.org/4814>.

### REFERENCES AND NOTES

- S. Herculano-Houzel, The human brain in numbers: A linearly scaled-up primate brain. *Front. Hum. Neurosci.* **3**, 31 (2009). doi: [10.3389/neuro.09.031.2009](https://doi.org/10.3389/neuro.09.031.2009); pmid: [19915731](https://pubmed.ncbi.nlm.nih.gov/19915731/)
- C. S. von Bartheld, J. Bahney, S. Herculano-Houzel, The search for true numbers of neurons and glial cells in the human brain: A review of 150 years of cell counting. *J. Comp. Neurol.* **524**, 3865–3895 (2016). doi: [10.1002/cne.24040](https://doi.org/10.1002/cne.24040); pmid: [27187682](https://pubmed.ncbi.nlm.nih.gov/27187682/)
- R. D. Hodge *et al.*, Conserved cell types with divergent features in human versus mouse cortex. *Nature* **573**, 61–68 (2019). doi: [10.1038/s41586-019-1506-7](https://doi.org/10.1038/s41586-019-1506-7); pmid: [31435019](https://pubmed.ncbi.nlm.nih.gov/31435019/)
- F. M. Krienen *et al.*, Innovations present in the primate interneuron repertoire. *Nature* **586**, 262–269 (2020). doi: [10.1038/s41586-020-2781-z](https://doi.org/10.1038/s41586-020-2781-z); pmid: [32999462](https://pubmed.ncbi.nlm.nih.gov/32999462/)
- K. Letinic, R. Zoncu, P. Rakic, Origin of GABAergic neurons in the human neocortex. *Nature* **417**, 645–649 (2002). doi: [10.1038/nature00779](https://doi.org/10.1038/nature00779); pmid: [12050665](https://pubmed.ncbi.nlm.nih.gov/12050665/)
- S. R. y. Cajal, Estudios sobre la corteza cerebral humana. II. Estructura de la corteza motriz del hombre y mamíferos superiores. *Revista Trimestral Micrográfica* **4**, 117–200 (1899).
- R. N. Kooijmans, W. Sierhuis, M. W. Self, P. R. Roelfsema, A quantitative comparison of inhibitory interneuron size and distribution between mouse and macaque V1, using calcium-binding proteins. *Cereb. Cortex Commun.* **1**, tga068 (2020). doi: [10.1093/texcom/tga068](https://doi.org/10.1093/texcom/tga068); pmid: [34296129](https://pubmed.ncbi.nlm.nih.gov/34296129/)
- J. Berg *et al.*, Human neocortical expansion involves glutamatergic neuron diversification. *Nature* **598**, 151–158 (2021). doi: [10.1038/s41586-021-03813-8](https://doi.org/10.1038/s41586-021-03813-8); pmid: [34616067](https://pubmed.ncbi.nlm.nih.gov/34616067/)
- T. E. Bakken *et al.*, Comparative cellular analysis of motor cortex in human, marmoset and mouse. *Nature* **598**, 111–119 (2021). doi: [10.1038/s41586-021-03465-8](https://doi.org/10.1038/s41586-021-03465-8); pmid: [34616062](https://pubmed.ncbi.nlm.nih.gov/34616062/)
- A. Shapson-Coe *et al.*, A connectomic study of a petascale fragment of human cerebral cortex. *bioRxiv*, 446289 [Preprint] (2021). doi: [10.1101/2021.05.29.446289](https://doi.org/10.1101/2021.05.29.446289)
- M. Field *et al.*, Tonic GABA<sub>A</sub> receptor-mediated currents of human cortical GABAergic interneurons vary amongst cell types. *J. Neurosci.* **41**, 9702–9719 (2021). doi: [10.1523/JNEUROSCI.0175-21.2021](https://doi.org/10.1523/JNEUROSCI.0175-21.2021); pmid: [34667071](https://pubmed.ncbi.nlm.nih.gov/34667071/)
- V. Szegedi *et al.*, Robust perisomatic GABAergic self-innervation inhibits basket cells in the human and mouse supragranular neocortex. *eLife* **9**, e51691 (2020). doi: [10.7554/eLife.51691](https://doi.org/10.7554/eLife.51691); pmid: [31916939](https://pubmed.ncbi.nlm.nih.gov/31916939/)
- A. M. M. Sousa *et al.*, Molecular and cellular reorganization of neural circuits in the human lineage. *Science* **358**, 1027–1032 (2017). doi: [10.1126/science.aan3456](https://doi.org/10.1126/science.aan3456); pmid: [29170230](https://pubmed.ncbi.nlm.nih.gov/29170230/)
- E. Boldog *et al.*, Transcriptomic and morphophysiological evidence for a specialized human cortical GABAergic cell type. *Nat. Neurosci.* **21**, 1185–1195 (2018). doi: [10.1038/s41593-018-0205-2](https://doi.org/10.1038/s41593-018-0205-2); pmid: [30150662](https://pubmed.ncbi.nlm.nih.gov/30150662/)
- J. DeFelipe, L. Alonso-Nanclares, J. I. Arellano, Microstructure of the neocortex: Comparative aspects. *J. Neurocytol.* **31**, 299–316 (2002). doi: [10.1023/A:1024130211265](https://doi.org/10.1023/A:1024130211265); pmid: [12815249](https://pubmed.ncbi.nlm.nih.gov/12815249/)
- A. Rollenhagen *et al.*, Synaptic organization of the human temporal lobe neocortex as revealed by high-resolution transmission, focused ion beam scanning, and electron microscopic tomography. *Int. J. Mol. Sci.* **21**, 5558 (2020). doi: [10.3390/ijms2115558](https://doi.org/10.3390/ijms2115558); pmid: [32756507](https://pubmed.ncbi.nlm.nih.gov/32756507/)
- M. Domínguez-Álvarez, M. Montero-Crespo, L. Blazquez-Llorca, J. DeFelipe, L. Alonso-Nanclares, 3D electron microscopy study of synaptic organization of the normal human transentorhinal cortex and its possible alterations in Alzheimer's disease. *eNeuro* **6**, ENEURO.0140-19.2019 (2019). doi: [10.1523/ENEURO.0140-19.2019](https://doi.org/10.1523/ENEURO.0140-19.2019); pmid: [31217195](https://pubmed.ncbi.nlm.nih.gov/31217195/)
- P. Marco, J. DeFelipe, Altered synaptic circuitry in the human temporal neocortex removed from epileptic patients. *Exp. Brain Res.* **114**, 1–10 (1997). doi: [10.1007/PL00005608](https://doi.org/10.1007/PL00005608); pmid: [9154464](https://pubmed.ncbi.nlm.nih.gov/9154464/)
- B. Wang *et al.*, A subtype of inhibitory interneuron with intrinsic persistent activity in human and monkey neocortex. *Cell Rep.* **10**, 1450–1458 (2015). doi: [10.1016/j.celrep.2015.02.018](https://doi.org/10.1016/j.celrep.2015.02.018); pmid: [25753411](https://pubmed.ncbi.nlm.nih.gov/25753411/)
- G. Molnár *et al.*, Complex events initiated by individual spikes in the human cerebral cortex. *PLOS Biol.* **6**, e222 (2008). doi: [10.1371/journal.pbio.0060222](https://doi.org/10.1371/journal.pbio.0060222); pmid: [18767905](https://pubmed.ncbi.nlm.nih.gov/18767905/)
- D. S. Melchitzky, S. R. Sesack, D. A. Lewis, Parvalbumin-immunoreactive axon terminals in macaque monkey and human prefrontal cortex: Laminar, regional, and target specificity of type I and type II synapses. *J. Comp. Neurol.* **408**, 11–22 (1999). doi: [10.1002/\(SICI\)1096-9861\(19990524\)408:1<11::AID-CNE1>3.0.CO;2-1](https://doi.org/10.1002/(SICI)1096-9861(19990524)408:1<11::AID-CNE1>3.0.CO;2-1); pmid: [10331577](https://pubmed.ncbi.nlm.nih.gov/10331577/)
- M. Domínguez-Álvarez, M. Montero-Crespo, L. Blazquez-Llorca, J. DeFelipe, L. Alonso-Nanclares, 3D ultrastructural study of synapses in the human entorhinal cortex. *Cereb. Cortex* **1**, 410–435 (2020).
- D. S. Melchitzky, D. A. Lewis, Dendritic-targeting GABA neurons in monkey prefrontal cortex: Comparison of somatostatin- and calretinin-immunoreactive axon terminals. *Synapse* **62**, 456–465 (2008). doi: [10.1002/syn.20514](https://doi.org/10.1002/syn.20514); pmid: [18361442](https://pubmed.ncbi.nlm.nih.gov/18361442/)
- N. Cano-Astorga, J. DeFelipe, L. Alonso-Nanclares, Three-dimensional synaptic organization of layer III of the human temporal neocortex, three-dimensional synaptic organization of layer III of the human temporal neocortex. *Cereb. Cortex* **31**, 4742–4764 (2021). doi: [10.1093/cercor/bhab120](https://doi.org/10.1093/cercor/bhab120); pmid: [33999122](https://pubmed.ncbi.nlm.nih.gov/33999122/)
- B. G. Cragg, Ultrastructural features of human cerebral cortex. *J. Anat.* **121**, 331–362 (1976). pmid: [179969](https://pubmed.ncbi.nlm.nih.gov/179969/)
- I. B. Yáñez *et al.*, Double bouquet cell in the human cerebral cortex and a comparison with other mammals. *J. Comp. Neurol.* **486**, 344–360 (2005). doi: [10.1002/cne.20533](https://doi.org/10.1002/cne.20533); pmid: [15846784](https://pubmed.ncbi.nlm.nih.gov/15846784/)
- E. A. Nimchinsky *et al.*, A neuronal morphologic type unique to humans and great apes. *Proc. Natl. Acad. Sci. U.S.A.* **96**, 5268–5273 (1999). doi: [10.1073/pnas.96.95268](https://doi.org/10.1073/pnas.96.95268); pmid: [10220455](https://pubmed.ncbi.nlm.nih.gov/10220455/)
- M. R. del Río, J. DeFelipe, Double bouquet cell axons in the human temporal neocortex: Relationship to bundles of myelinated axons and colocalization of calretinin and calbindin D-28k immunoreactivities. *J. Chem. Neuroanat.* **13**, 243–251 (1997). doi: [10.1016/S0891-0618\(97\)00050-1](https://doi.org/10.1016/S0891-0618(97)00050-1); pmid: [9412906](https://pubmed.ncbi.nlm.nih.gov/9412906/)
- R. Benavides-Piccione, I. Ballesteros-Yáñez, J. DeFelipe, R. Yuste, Cortical area and species differences in dendritic spine morphology. *J. Neurocytol.* **31**, 337–346 (2002). doi: [10.1023/A:1024134312173](https://doi.org/10.1023/A:1024134312173); pmid: [12815251](https://pubmed.ncbi.nlm.nih.gov/12815251/)
- V. Szegedi *et al.*, Plasticity in Single Axon Glutamatergic Connection to GABAergic Interneurons Requires Complex Events in the Human Neocortex. *PLOS Biol.* **14**, e2000237 (2016). doi: [10.1371/journal.pbio.2000237](https://doi.org/10.1371/journal.pbio.2000237); pmid: [27828957](https://pubmed.ncbi.nlm.nih.gov/27828957/)
- K. D. Micheva, C. Beaulieu, Postnatal development of GABA neurons in the rat somatosensory barrel cortex: A quantitative study. *Eur. J. Neurosci.* **7**, 419–430 (1995). doi: [10.1111/j.1460-9568.1995.tb00338.x](https://doi.org/10.1111/j.1460-9568.1995.tb00338.x); pmid: [7773439](https://pubmed.ncbi.nlm.nih.gov/7773439/)
- H. S. Meyer *et al.*, Inhibitory interneurons in a cortical column form hot zones of inhibition in layers 2 and 5A. *Proc. Natl. Acad. Sci. U.S.A.* **108**, 16807–16812 (2011). doi: [10.1073/pnas.1113648108](https://doi.org/10.1073/pnas.1113648108); pmid: [21949377](https://pubmed.ncbi.nlm.nih.gov/21949377/)
- D. Djäja, A. Hladnik, I. Bičanić, M. Baković, Z. Petanjek, Neocortical calretinin neurons in primates: Increase in proportion and microcircuitry structure. *Front. Neuroanat.* **8**, 103–103 (2014). pmid: [25309344](https://pubmed.ncbi.nlm.nih.gov/25309344/)
- B. Tasic *et al.*, Shared and distinct transcriptomic cell types across neocortical areas. *Nature* **563**, 72–78 (2018). doi: [10.1038/s41586-018-0654-5](https://doi.org/10.1038/s41586-018-0654-5); pmid: [30382198](https://pubmed.ncbi.nlm.nih.gov/30382198/)
- J. Q. Ren, Y. Aika, C. W. Heizmann, T. Kosaka, Quantitative analysis of neurons and glial cells in the rat somatosensory cortex, with special reference to GABAergic neurons and parvalbumin-containing neurons. *Exp. Brain Res.* **92**, 1–14 (1992). doi: [10.1007/BF00230378](https://doi.org/10.1007/BF00230378); pmid: [1486945](https://pubmed.ncbi.nlm.nih.gov/1486945/)
- C. Beaulieu, G. Campistron, C. Crevier, Quantitative aspects of the GABA circuitry in the primary visual cortex of the adult rat. *J. Comp. Neurol.* **339**, 559–572 (1994). doi: [10.1002/cne.903390407](https://doi.org/10.1002/cne.903390407); pmid: [8144746](https://pubmed.ncbi.nlm.nih.gov/8144746/)
- S. Lefort, C. Tomm, J. C. Floyd Sarria, C. C. H. Petersen, The excitatory neuronal network of the C2 barrel column in mouse primary somatosensory cortex. *Neuron* **61**, 301–316 (2009). doi: [10.1016/j.neuron.2008.12.020](https://doi.org/10.1016/j.neuron.2008.12.020); pmid: [19186171](https://pubmed.ncbi.nlm.nih.gov/19186171/)
- C. Beaulieu, Z. Kisvarday, P. Somogyi, M. Cynader, A. Cowey, Quantitative distribution of GABA-immunopositive and -immunonegative neurons and synapses in the monkey striate cortex (area 17). *Cereb. Cortex* **2**, 295–309 (1992). doi: [10.1093/cercor/2.4.295](https://doi.org/10.1093/cercor/2.4.295); pmid: [1330121](https://pubmed.ncbi.nlm.nih.gov/1330121/)
- P. L. A. Gabbott, S. J. Bacon, Local circuit neurons in the medial prefrontal cortex (areas 24a,b,c, 25 and 32) in the monkey: I. Cell morphology and morphometrics. *J. Comp. Neurol.* **364**, 567–608 (1996). doi: [10.1002/\(SICI\)1096-9861\(19960122\)364:4<567::AID-CNE1>3.0.CO;2-1](https://doi.org/10.1002/(SICI)1096-9861(19960122)364:4<567::AID-CNE1>3.0.CO;2-1); pmid: [8821449](https://pubmed.ncbi.nlm.nih.gov/8821449/)
- J.-P. Hornung, N. De Tribolet, Distribution of GABA-containing neurons in human frontal cortex: A quantitative immunocytochemical study. *Anat. Embryol.* **189**, 139–145 (1994). doi: [10.1007/BF00185772](https://doi.org/10.1007/BF00185772); pmid: [8010412](https://pubmed.ncbi.nlm.nih.gov/8010412/)
- M. R. del Río, J. DeFelipe, Colocalization of calbindin D-28k, calretinin, and GABA immunoreactivities in neurons of the human temporal cortex. *J. Comp. Neurol.* **369**, 472–482 (1996). doi: [10.1002/\(SICI\)1096-9861\(19960603\)369:3<472::AID-CNE11>3.0.CO;2-K](https://doi.org/10.1002/(SICI)1096-9861(19960603)369:3<472::AID-CNE11>3.0.CO;2-K); pmid: [8743426](https://pubmed.ncbi.nlm.nih.gov/8743426/)
- E. G. Jones, G. W. Huntley, D. L. Benson, Alpha calcium/calmodulin-dependent protein kinase II selectively expressed in a subpopulation of excitatory neurons in monkey sensory

- motor cortex: Comparison with GAD-67 expression. *J. Neurosci.* **14**, 611–629 (1994). doi: [10.1523/JNEUROSCI.14-02-00611.1994](https://doi.org/10.1523/JNEUROSCI.14-02-00611.1994); pmid: [8301355](#)
43. G. Eyal *et al.*, Human cortical pyramidal neurons: From spines to spikes via models. *Front. Cell. Neurosci.* **12**, 181 (2018). doi: [10.3389/fncel.2018.00181](https://doi.org/10.3389/fncel.2018.00181); pmid: [30008663](#)
44. R. Benavides-Piccione, I. Fernaud-Espinosa, V. Robles, R. Yuste, J. DeFelipe, Age-based comparison of human dendritic spine structure using complete three-dimensional reconstructions. *Cereb. Cortex* **23**, 1798–1810 (2013). doi: [10.1093/cercor/bhs154](https://doi.org/10.1093/cercor/bhs154); pmid: [22710613](#)
45. H. Mohan *et al.*, Dendritic and axonal architecture of individual pyramidal neurons across layers of adult human neocortex. *Cereb. Cortex* **25**, 4839–4853 (2015). doi: [10.1093/cercor/bhv188](https://doi.org/10.1093/cercor/bhv188); pmid: [26318661](#)
46. G. N. Elston, R. Benavides-Piccione, J. DeFelipe, The pyramidal cell in cognition: A comparative study in human and monkey. *J. Neurosci.* **21**, RC163–RC163 (2001). doi: [10.1523/JNEUROSCI.21-17-j0002.2001](https://doi.org/10.1523/JNEUROSCI.21-17-j0002.2001); pmid: [11511694](#)
47. M. B. Ramocki, H. Y. Zoghbi, Failure of neuronal homeostasis results in common neuropsychiatric phenotypes. *Nature* **455**, 912–918 (2008). doi: [10.1038/nature07457](https://doi.org/10.1038/nature07457); pmid: [18923513](#)
48. J. L. R. Rubenstein, M. M. Merzenich, Model of autism: Increased ratio of excitation/inhibition in key neural systems. *Genes Brain Behav.* **2**, 255–267 (2003). doi: [10.1034/j.1601-183X.2003.00037.x](https://doi.org/10.1034/j.1601-183X.2003.00037.x); pmid: [16066691](#)
49. A. Motta *et al.*, Dense connectomic reconstruction in layer 4 of the somatosensory cortex. *Science* **366**, eaay3134 (2019). doi: [10.1126/science.aay3134](https://doi.org/10.1126/science.aay3134); pmid: [31649140](#)
50. W. Denk, H. Horstmann, Serial block-face scanning electron microscopy to reconstruct three-dimensional tissue nanostructure. *PLOS Biol.* **2**, e329 (2004). doi: [10.1371/journal.pbio.0020329](https://doi.org/10.1371/journal.pbio.0020329); pmid: [15514700](#)
51. K. J. Hayworth *et al.*, Imaging ATUM ultrathin section libraries with WaferMapper: A multi-scale approach to EM reconstruction of neural circuits. *Front. Neural Circuits* **8**, 68 (2014). doi: [10.3389/fncir.2014.00068](https://doi.org/10.3389/fncir.2014.00068); pmid: [25018701](#)
52. K. J. Hayworth, N. Kashuri, R. Schalek, J. W. Lichtman, Automating the collection of ultrathin serial sections for large volume TEM reconstructions. *Microsc. Microanal.* **12** (S02), 86–87 (2006). doi: [10.1017/S1431927606066268](https://doi.org/10.1017/S1431927606066268)
53. A. L. Eberle *et al.*, High-resolution, high-throughput imaging with a multibeam scanning electron microscope. *J. Microsc.* **259**, 114–120 (2015). doi: [10.1111/jmi.12224](https://doi.org/10.1111/jmi.12224); pmid: [25627873](#)
54. K. Lee, J. Zung, P. Li, V. Jain, H. S. Seung, Superhuman accuracy on the SNEMI3D connectomics challenge. [arXiv:1706.00120v1 \[cs.CV\]](https://arxiv.org/abs/1706.00120v1) (2017).
55. A. Karimi, J. Odenthal, F. Drawitsch, K. M. Boergens, M. Helmstaedter, Cell-type specific innervation of cortical pyramidal cells at their apical dendrites. *eLife* **9**, e46876 (2020). doi: [10.7554/eLife.46876](https://doi.org/10.7554/eLife.46876); pmid: [32108571](#)
56. V. Braibantov, A. Schütz, *Cortex: Statistics and Geometry of Neuronal Connectivity* (Springer Science & Business Media, 1998).
57. T. Kwon *et al.*, Ultrastructural, molecular and functional mapping of GABAergic synapses on dendritic spines and shafts of neocortical pyramidal neurons. *Cereb. Cortex* **29**, 2771–2781 (2019). doi: [10.1093/cercor/bhy143](https://doi.org/10.1093/cercor/bhy143); pmid: [30113619](#)
58. Y. Kubota, F. Karube, M. Nomura, Y. Kawaguchi, The diversity of cortical inhibitory synapses. *Front. Neural Circuits* **10**, 27–27 (2016). doi: [10.3389/fncir.2016.00027](https://doi.org/10.3389/fncir.2016.00027); pmid: [27199670](#)
59. G. A. Wildenberg *et al.*, Primate neuronal connections are sparse in cortex as compared to mouse. *Cell Rep.* **36**, 109709 (2021). doi: [10.1016/j.celrep.2021.109709](https://doi.org/10.1016/j.celrep.2021.109709); pmid: [34525373](#)
60. A. T. Kuan *et al.*, Dense neuronal reconstruction through x-ray holographic nano-tomography. *Nat. Neurosci.* **23**, 1637–1643 (2020). doi: [10.1038/s41593-020-0704-9](https://doi.org/10.1038/s41593-020-0704-9); pmid: [32929244](#)
61. Y. Kubota, S. Hatada, S. Kondo, F. Karube, Y. Kawaguchi, Neocortical inhibitory terminals innervate dendritic spines targeted by thalamocortical afferents. *J. Neurosci.* **27**, 1139–1150 (2007). doi: [10.1523/JNEUROSCI.3846-06-2007](https://doi.org/10.1523/JNEUROSCI.3846-06-2007); pmid: [17267569](#)
62. M. R. del Rio, J. DeFelipe, A light and electron microscopic study of calbindin D-28k immunoreactive double bouquet cells in the human temporal cortex. *Brain Res.* **690**, 133–140 (1995). doi: [10.1016/0006-8993\(95\)00641-3](https://doi.org/10.1016/0006-8993(95)00641-3); pmid: [7496800](#)
63. I. P. Lukacs *et al.*, Differential effects of group III metabotropic glutamate receptors on spontaneous inhibitory synaptic currents in spine-innervating double bouquet and parvalbumin-expressing dendrite-targeting GABAergic interneurons in human neocortex. *bioRxiv*, 483105 [Preprint] (2022). doi: [10.1101/2022.03.05.483105](https://doi.org/10.1101/2022.03.05.483105)
64. C. Xu *et al.*, Structure and plasticity of silent synapses in developing hippocampal neurons visualized by super-resolution imaging. *Cell Discov.* **6**, 8 (2020). doi: [10.1038/s41421-019-0139-1](https://doi.org/10.1038/s41421-019-0139-1); pmid: [32133151](#)
65. G. M. Durand, Y. Kovalchuk, A. Konnerth, Long-term potentiation and functional synapse induction in developing hippocampus. *Nature* **381**, 71–75 (1996). doi: [10.1038/381071a0](https://doi.org/10.1038/381071a0); pmid: [8609991](#)
66. M. Lenz *et al.*, All-trans retinoic acid induces synaptic plasticity in human cortical neurons. *eLife* **10**, e63026 (2021). doi: [10.7554/eLife.63026](https://doi.org/10.7554/eLife.63026); pmid: [33781382](#)
67. H. Schmidt *et al.*, Axonal synapse sorting in medial entorhinal cortex. *Nature* **549**, 469–475 (2017). doi: [10.1038/nature24005](https://doi.org/10.1038/nature24005); pmid: [28959971](#)
68. J. Kornfeld *et al.*, EM connectomics reveals axonal target variation in a sequence-generating network. *eLife* **6**, e24364 (2017). doi: [10.7554/eLife.24364](https://doi.org/10.7554/eLife.24364); pmid: [28346140](#)
69. C. E. Carr, M. Konishi, A circuit for detection of interaural time differences in the brain stem of the barn owl. *J. Neurosci.* **10**, 3227–3246 (1990). doi: [10.1523/JNEUROSCI.10-10-03227.1990](https://doi.org/10.1523/JNEUROSCI.10-10-03227.1990); pmid: [2213141](#)
70. K. D. Micheva, C. Beaulieu, Quantitative aspects of synaptogenesis in the rat barrel field cortex with special reference to GABA circuitry. *J. Comp. Neurol.* **373**, 340–354 (1996). doi: [10.1002/\(SICI\)1096-9861\(19960923\)373:3<340::AID-CNE3>3.0.CO;2-2](https://doi.org/10.1002/(SICI)1096-9861(19960923)373:3<340::AID-CNE3>3.0.CO;2-2); pmid: [8889932](#)
71. C. Cali *et al.*, The effects of aging on neuropil structure in mouse somatosensory cortex-A 3D electron microscopy analysis of layer 1. *PLOS ONE* **13**, e0198131 (2018). doi: [10.1371/journal.pone.0198131](https://doi.org/10.1371/journal.pone.0198131); pmid: [29966021](#)
72. J. P. Bourgeois, P. Rakic, Changes of synaptic density in the primary visual cortex of the macaque monkey from fetal to adult stage. *J. Neurosci.* **13**, 2801–2820 (1993). doi: [10.1523/JNEUROSCI.13-07-02801.1993](https://doi.org/10.1523/JNEUROSCI.13-07-02801.1993); pmid: [8331373](#)
73. S. A. Kirov, L. J. Petruk, J. C. Fiala, K. M. Harris, Dendritic spines disappear with chilling but proliferate excessively upon rewarming of mature hippocampus. *Neuroscience* **127**, 69–80 (2004). doi: [10.1016/j.neuroscience.2004.04.053](https://doi.org/10.1016/j.neuroscience.2004.04.053); pmid: [15219670](#)
74. L. A. Glantz, D. A. Lewis, Decreased dendritic spine density on prefrontal cortical pyramidal neurons in schizophrenia. *Arch. Gen. Psychiatry* **57**, 65–73 (2000). doi: [10.1001/archpsyc.57.1.65](https://doi.org/10.1001/archpsyc.57.1.65); pmid: [10632234](#)
75. M. Medalla, J. P. Gilman, J.-Y. Wang, J. I. Luebke, Strength and diversity of inhibitory signaling differentiates primate anterior cingulate from lateral prefrontal cortex. *J. Neurosci.* **37**, 4717–4734 (2017). doi: [10.1523/JNEUROSCI.3757-16.2017](https://doi.org/10.1523/JNEUROSCI.3757-16.2017); pmid: [28381592](#)
76. A. Hsu, J. I. Luebke, M. Medalla, Comparative ultrastructural features of excitatory synapses in the visual and frontal cortices of the adult mouse and monkey. *J. Comp. Neurol.* **525**, 2175–2191 (2017). doi: [10.1002/cne.24196](https://doi.org/10.1002/cne.24196); pmid: [28256708](#)
77. J. P. Gilman, M. Medalla, J. I. Luebke, Area-specific features of pyramidal neurons-a comparative study in mouse and rhesus monkey. *Cereb. Cortex* **27**, 2078–2094 (2017). doi: [10.1002/cne.24196](https://doi.org/10.1002/cne.24196); pmid: [26965903](#)
78. A. Gidon *et al.*, Dendritic action potentials and computation in human layer 2/3 cortical neurons. *Science* **367**, 83–87 (2020). doi: [10.1126/science.aax6239](https://doi.org/10.1126/science.aax6239); pmid: [31896716](#)
79. G. Eyal *et al.*, Unique membrane properties and enhanced signal processing in human neocortical neurons. *eLife* **5**, e16553 (2016). doi: [10.7554/eLife.16553](https://doi.org/10.7554/eLife.16553); pmid: [2710767](#)
80. B. Scholl, C. I. Thomas, M. A. Ryan, N. Kamasawa, D. Fitzpatrick, Cortical response selectivity derives from strength in numbers of synapses. *Nature* **590**, 111–114 (2021). doi: [10.1038/s41586-020-03044-3](https://doi.org/10.1038/s41586-020-03044-3); pmid: [3328635](#)
81. J. J. Letzkus *et al.*, A disinhibitory microcircuit for associative fear learning in the auditory cortex. *Nature* **480**, 331–335 (2011). doi: [10.1038/nature10674](https://doi.org/10.1038/nature10674); pmid: [22158104](#)
82. J. J. Letzkus, S. B. E. Wolff, A. Lüthi, Disinhibition, a circuit mechanism for associative learning and memory. *Neuron* **88**, 264–276 (2015). doi: [10.1016/j.neuron.2015.09.024](https://doi.org/10.1016/j.neuron.2015.09.024); pmid: [26494276](#)
83. R. Kim, T. J. Sejnowski, Strong inhibitory signaling underlies stable temporal dynamics and working memory in spiking neural networks. *Nat. Neurosci.* **24**, 129–139 (2021). doi: [10.1038/s41589-00753-w](https://doi.org/10.1038/s41589-00753-w); pmid: [33288909](#)
84. A. Gout *et al.*, Postnatal connectome development of inhibition in mouse barrel cortex. *Science* **371**, eabb4534 (2021). doi: [10.1126/science.abb4534](https://doi.org/10.1126/science.abb4534); pmid: [33273061](#)
85. Y. Hua, P. Laserstein, M. Helmstaedter, Large-volume en-bloc staining for electron microscopy-based connectomics. *Nat. Commun.* **6**, 7923 (2015). doi: [10.1038/ncomms8923](https://doi.org/10.1038/ncomms8923); pmid: [26235643](#)
86. F. Drawitsch, A. Karimi, K. M. Boergens, M. Helmstaedter, FluoEM, virtual labeling of axons in three-dimensional electron microscopy data for long-range connectomics. *eLife* **7**, e38976 (2018). doi: [10.7554/eLife.38976](https://doi.org/10.7554/eLife.38976); pmid: [30106377](#)
87. K. M. Boergens *et al.*, webKnossos: Efficient online 3D data annotation for connectomics. *Nat. Methods* **14**, 691–694 (2017). doi: [10.1038/nmeth.4331](https://doi.org/10.1038/nmeth.4331); pmid: [28604722](#)
88. M. A. Fischler, R. C. Bolles, Random sample consensus: A paradigm for model fitting with applications to image analysis and automated cartography. *Commun. ACM* **24**, 381–395 (1981). doi: [10.1145/358669.358692](https://doi.org/10.1145/358669.358692)
89. L. K. Scheffer, B. Karsh, S. Vitaladevun, Automated alignment of imperfect EM images for neural reconstruction. [arXiv:1304.6034v1 \[q-bio.QM\]](https://arxiv.org/abs/1304.6034v1) (2013).
90. A. Peters, Cellular components of the cerebral cortex, in *Cerebral Cortex* (Univ. Chicago Press, 1984), vol. 1, pp. 107–200.
91. P. Somogyi, A. Cowey, Combined Golgi and electron microscopic study on the synapses formed by double bouquet cells in the visual cortex of the cat and monkey. *J. Comp. Neurol.* **195**, 547–566 (1981). doi: [10.1002/cne.901950402](https://doi.org/10.1002/cne.901950402); pmid: [7462443](#)
92. A. D. de Lima, J. H. Morrison, Ultrastructural analysis of somatostatin-immunoreactive neurons and synapses in the temporal and occipital cortex of the macaque monkey. *J. Comp. Neurol.* **283**, 212–227 (1989). doi: [10.1002/cne.902830205](https://doi.org/10.1002/cne.902830205); pmid: [2567743](#)
93. J. DeFelipe, S. H. Hendry, E. G. Jones, Synapses of double bouquet cells in monkey cerebral cortex visualized by calbindin immunoreactivity. *Brain Res.* **503**, 49–54 (1989). doi: [10.1016/0006-8993\(89\)91702-2](https://doi.org/10.1016/0006-8993(89)91702-2); pmid: [2611658](#)
94. J. DeFelipe, S. H. Hendry, T. Hashikawa, M. Molinari, E. G. Jones, A microcolumnar structure of monkey cerebral cortex revealed by immunocytochemical studies of double bouquet cell axons. *Neuroscience* **37**, 655–673 (1990). doi: [10.1016/0306-4522\(90\)90097-N](https://doi.org/10.1016/0306-4522(90)90097-N); pmid: [1701039](#)
95. P. Somogyi, T. F. Freund, A. Cowey, The axo-axonic interneuron in the cerebral cortex of the rat, cat and monkey. *Neuroscience* **7**, 2577–2607 (1982). doi: [10.1016/0306-4522\(82\)90086-0](https://doi.org/10.1016/0306-4522(82)90086-0); pmid: [7155343](#)
96. B. Cauli *et al.*, Molecular and physiological diversity of cortical nonpyramidal cells. *J. Neurosci.* **17**, 3894–3906 (1997). doi: [10.1523/JNEUROSCI.17-10-03894.1997](https://doi.org/10.1523/JNEUROSCI.17-10-03894.1997); pmid: [9133407](#)
97. Y. Kawaguchi, Y. Kubota, Physiological and morphological identification of somatostatin- or vasoactive intestinal polypeptide-containing cells among GABAergic cell subtypes in rat frontal cortex. *J. Neurosci.* **16**, 2701–2715 (1996). doi: [10.1523/JNEUROSCI.16-08-02701.1996](https://doi.org/10.1523/JNEUROSCI.16-08-02701.1996); pmid: [8786446](#)
98. C. K. Pfeffer, M. Xue, M. He, Z. J. Huang, M. Scanziani, Inhibition of inhibition in visual cortex: The logic of connections between molecularly distinct interneurons. *Nat. Neurosci.* **16**, 1068–1076 (2013). doi: [10.1038/nrn.3446](https://doi.org/10.1038/nrn.3446); pmid: [23817549](#)
99. B. Efron, Bootstrap methods: Another look at the jackknife. *Ann. Stat.* **7**, 1–26 (1979). doi: [10.1214/aos/1176344552](https://doi.org/10.1214/aos/1176344552)
100. S. B. Hedges, S. Kumar, Genomics. Vertebrate genomes compared. *Science* **297**, 1283–1285 (2002). doi: [10.1126/science.1076231](https://doi.org/10.1126/science.1076231); pmid: [12193771](#)
101. M. A. Hofman, Evolution of the human brain: When bigger is better. *Front. Neuroanat.* **8**, 15 (2014). doi: [10.3389/fnana.2014.00015](https://doi.org/10.3389/fnana.2014.00015); pmid: [24723857](#)

**ACKNOWLEDGMENTS**

We thank K. Matz-Rensing at the German Primate Center and F. Bremmer and A. Kaminiarz at the University of Marburg for providing tissue of macaque brain; anonymous individuals H5 and H6 for consent to provide tissue from neurosurgery interventions; H. Wissler for support with visualizations and for management of the neuron reconstruction team; I. Wolf and J. Kim for staining support; A. Karimi, F. Drawitsch, and K. M. Boergens for providing custom written image acquisition and alignment routines; S. Babl, L. Bezzemberger, R. Jakoby, R. Kneisl, and M. Kronawitter for annotator training and task management; D. Werner, V. Pirkau, G. Wiese, F. Meinel, J. Striebel, P. Otto, T. Herold, and N. Rzepka at scalable minds, Potsdam, Germany for collaboration on automated data analysis; T. Garbowksi and D. Lechner (Zeiss) for help with setting up multiSEM; M. Fahland and N. Prager (Fraunhofer FEP, Dresden) for collaboration on Kapton tape; R. Schalek and J. Lichtman for initial advice on setting up ATUM; G. Tushav, A. Kotowicz, T. Zeller, and C. Guggenberger for IT support; S. Soworka, I. Wolf, S. Horn and L. Dadashov for excellent technical support; and three anonymous reviewers for helpful advice. Additional methodological acknowledgments are provided in the supplementary materials.

**Funding:** Funding was provided by the Max-Planck Society. S.L. was partly funded by Neuronex2 grant (DFG, German Research Foundation–HE 7321/1-1). **Author contributions:** M.H. conceived, initiated and supervised the study. J.S., N.H., A.M.K., V.G., and N.J. carried out experiments. H.S.M. and J.G. provided human tissue. M.S. provided ATUM-multiSEM methodology. A.M. developed and applied analysis methodology. S.L., J.S., N.H., A.M.K., V.G., and M.H. provided reconstructions and analyzed data. S.L. and M.H. wrote the manuscript, with contributions from all authors. **Competing interests:** The authors declare no competing financial interests.

**Data and materials availability:** All image data and reconstructions are publicly available through <https://www.webknossos.org> under the links at the end of the Materials and methods section. All software used for analysis is available at the following address and have been made publicly available under the MIT license: [https://gitlab.mpcdf.mpg.de/connectomics/human\\_primate](https://gitlab.mpcdf.mpg.de/connectomics/human_primate). **License information:** Copyright © 2022 the authors, some rights reserved; exclusive licensee American Association for the Advancement of Science. No claim to original US government works. <https://www.science.org/about/science-licenses-journal-article-reuse>

## SUPPLEMENTARY MATERIALS

[science.org/doi/10.1126/science.abo0924](https://science.org/doi/10.1126/science.abo0924)

Materials and Methods

Supplementary Text

Figs. S1 to S4

MDAR Reproducibility Checklist

Submitted 13 January 2022; accepted 30 May 2022

Published online 23 June 2022

10.1126/science.abo0924